# Bayesian multi-model estimation for fault slip distribution: the effect of prior constraints in the estimation for slow slip events beneath the Bungo Channel, southwest Japan

**R. Agata[1], R. Nakata[2], A. Kasahara[3], Y. Yagi[4], Y. Seshimo[5], S. Yoshioka[6,5], T. Iinuma[1]**

[1]Japan Agency for Marine-Earth Science and Technology, 3173-25 Showa-machi, Kanazawa-ku, Yokohama 236-0001, Japan
[2]Graduate School of Science, Tohoku University, 6-6 Aramaki-aza-aoba, Aoba-ku, Sendai 980-8578, Japan
[3]Independent researcher
[4]Faculty of Life and Environmental Sciences, University of Tsukuba, 1-1-1 Tennodai, Tsukuba-shi, Ibaraki 305-8572, Japan
[5]Department of Planetology, Graduate School of Science, Kobe University, 1-1 Rokkodai-cho, Nada-ku, Kobe, Hyogo, Japan, 657-8501, Japan
[6]Research Center for Urban Safety and Security, Kobe University, 1-1 Rokkodai-cho, Nada-ku, Kobe 657-8501, Japan

**Key Points:**

- Fault slip distributions in slow slip events (SSE) at southwest Japan were estimated considering the uncertainty of underground structure
- The results suggested the mechanical relationship between the SSEs and synchronized tectonic tremors more clearly than previous ones
- Sequential estimates of fault slips in repeating SSEs by reducing the model uncertainty resulted in a preferable Bayesian inference

Corresponding author: Ryoichiro Agata, `agatar@jamstec.go.jp`

## Abstract

We consider a Bayesian multi-model fault slip estimation (BMMFSE), in which many candidates of the underground-structure model characterized by a prior probability density function (PDF) are retained for a fully Bayesian estimation of fault slip distribution to manage model uncertainty properly. We performed geodetic data inversions to estimate slip distribution in long-term slow slip events (L-SSEs) that occurred beneath the Bungo Channel, southwest Japan, in around 2010 and 2018, focusing on the two advantages of BMMFSE: First, it allows for estimating slip distribution without introducing strong prior information such as smoothing constraints, handling an ill-posed inverse problem by combining a full Bayesian inference and accurate consideration of model uncertainty to avoid overfitting; second, the posterior PDF for the underground structure is also obtained through a fault slip estimation, which enables the estimation of sequential events by reducing the model uncertainty. The estimated slip distribution obtained using BMMFSE agreed better with the distribution of deep tectonic tremors at the down-dip side of the main rupture area than those obtained based on strong prior constraints in terms of the spatial distribution of the Coulomb failure stress change. This finding suggests a mechanical relationship between the L-SSE and the synchronized tremors. The use of the posterior PDF for the underground structure updated by the estimation for the 2010 L-SSE as an input of the analysis for the one in 2018 resulted in a more preferable Bayesian inference, indicated by a smaller value of an information criterion.



## Plain Language Summary

This study attempts to accurately estimate moves between two plates for the occurrence of slow slip events (SSEs), which are slow earthquakes that do not produce seismic waves, targeting those occurred in southwest Japan. This was accomplished by analyzing satellite data of ground movement during the SSEs using a novel approach called the Bayesian multi-model fault slip estimation (BMMFSE) framework, which considers multiple candidates of assumptions for Earth structures. BMMFSE stabilizes the analysis and removes artifacts from the estimation results which are otherwise introduced because of the choice of a wrong Earth model. These advantages were validated by comparing the estimation results obtained based on previous approaches that do not consider multiple Earth models. The result of BMMFSE exhibited spatial distributions of fault moves that are more consistent with other slow earthquakes which occurred synchronously in the nearby fault. The method also sequentially revised the multiple Earth models and produced a better ensemble of the candidate models through the analyses of repeating SSEs.


## 1 Introduction

Accurately estimating slip distribution using seismic waveforms and geodetic data is essential to better understand earthquake rupture and preparation processes underground, such as interplate coupling. Recent advances in seismological and geodetic observation techniques have led to the recognition of a new class of fault slip that is transitional between the fast rupture and stable sliding on the plate interface, which are known as slow earthquakes. Slow slip event (SSE) is a type of slow earthquake whose characteristic time scale is days (short-term SSE or S-SSE) to years (long-term SSE or L-SSE). The response signal of an SSE is usually detectable by geodetic measurements (Obara & Kato, 2016), from which the slip distribution can be inferred. The occurrence of both L-SSEs and S-SSEs is often accompanied by an increase in the number of smaller events, in terms of both the amount of seismic moment release and the time scale, in the surrounding area.

For example, there have been many observations of S-SSEs associated with deep tectonic tremors, known as episodic tremor and slips (ETS) (e.g., Cascadia subduction zone (Rogers & Dragert, 2003), Nankai trough subduction zone (Obara et al., 2004), etc.). Some L-SSEs are known to induce an increase in the number of surrounding tremors (e.g., the Bungo Channel in southwest Japan (Hirose et al., 2010), the Guerrero subduction zone (Kostoglodov et al., 2010; Villafuerte & Cruz-Atienza, 2017), etc.), and swarm-like seismic activities (for example, the Boso Peninsula in central Japan (Hirose et al., 2014), and the Hikurangi subduction zone (Bartlow et al., 2014). To investigate the generation process of slow earthquakes, spatial relationships between the estimated slip distribution for SSEs and hypocenter locations of such small events have been particularly studied (the readers are referred to the aforementioned articles). In addition, slip distribution occurring in SSEs that occur repeatedly in the same region has been analyzed simultaneously (Bartlow et al. (2014); Yoshioka et al. (2015); Takagi et al. (2019); Hirose and Kimura (2020) and many others), in part because the interval between each event is relatively short compared to ordinary earthquakes of the same level of seismic moment release. Comparisons of slip distributions in such repeating events may be useful for detecting temporal changes in the interseismic coupling rate or stress conditions in the surrounding seismogenic zones.

## 1.1 Fauls slip estimation and uncertainty of the underground structure

Regardless of targeting ordinary earthquakes or SSEs, the estimation of fault slip distribution is usually performed in a two-step procedure (e.g., pointed out by Fukahata and Matsu'ura (2006)): The first step is to set a numerical model that describes the characteristics of the media in the target domain of the Earth. A numerical model of the underground structure (which in principle consists of an elastic structure and the geometry of the fault plane in this study) is assumed by referring to databases proposed by previous studies based on many observations. In parametrizing the slip distribution in the assumed underground structure model, the slip parameters and the response at the observation points are usually described by a linear relationship (in many cases, based on linear elasticity). In the second step, the parameters that describe the slip distribution are estimated using observation data based on a linear relationship. This approach assumes that the earth model is associated with no uncertainty because a single underground structure model is chosen in the first step and other possibilities for model selection are discarded. This assumption allows for simplification by formulating the slip estimation as a simple linear inverse problem, which has been widely applied in previous studies. However, such an assumption often underestimates the amount of error in the prediction made by the model, which can lead to overfitting in estimation and obtaining a biased estimation result (e.g., Yagi and Fukahata (2008, 2011)).

To avoid such overfitting and bias in estimations, some approaches for considering model uncertainty in fault slip estimation have been proposed. The most straightforward approach is to estimate the parameters of the slip distribution and those that characterize the underground structure simultaneously (e.g., Fukahata and Wright (2008); Fukuda and Johnson (2010); Minson et al. (2014); Agata et al. (2018); Shimizu et al. (2021)). Another approach is to introduce the contribution of the model prediction errors to the covariance components in the data covariance matrix. Yagi and Fukahata (2011) proposed an inversion scheme that introduces the error of Green's functions following a Gaussian distribution and iteratively estimates the model parameters and the covariance matrix for the model prediction errors simultaneously. Duputel et al. (2014) proposed a comprehensive framework to compute the covariance matrix that considers the stochastic property of model prediction errors based on uncertain and presumably inaccurate prior knowledge of the underground elastic structure. These methods are known to relax the effect of overfitting in the estimation of fault slip distribution owing to the choice of a single underground structure model. However, the former approach based on simultaneous estimation usually adds unknowns that are in a nonlinear relationship with the response in observation stations to the target estimation problem. In such a case, it is necessary to perform the forward simulation iteratively to obtain a converged solution. The calculation cost associated with iterative analysis may limit the range of applicable problems. The latter approach, which introduces the covariance components, retains a linear relationship between unknown parameters and the observation response, which avoids iterative executions of the forward simulation within the estimation scheme. However, this approach procures no information on the underground structure that is intrinsically included in the data. In addition, it is based on the assumption that the model prediction errors follow a Gaussian distribution, which may be violated when the model uncertainty is large.

Recently, Agata et al. (2021) proposed a flexible framework of Bayesian inference for slip estimation considering model uncertainty, which introduces many candidates for underground structure models, whose characteristic parameters follow a prior probability density function (PDF), instead of choosing a single model in the "first step" of the process of a usual fault slip inversion. This approach allows for the estimation of slip parameters considering a wider range of underground structure parameters while avoiding non-linear parameters to be included in the estimation. Such treatment is enabled by eliminating the underground structure parameters by marginalization in advance of Bayesian sampling for the posterior PDF of the slip parameters. Furthermore, the posterior PDF for the underground structure can be obtained in a post process of Bayesian sampling. In addition, the formulation of the work corresponds to the generalization of the one proposed in Duputel et al. (2014) in that the framework of Agata et al. (2021) is not limited to applications assuming the Gaussian distribution but allows for an arbitrary probability distribution by using an ensemble approximation. We can also interpret the framework in the context of Bayesian multi-model estimation, originally called Bayesian model averaging (Raftery et al., 1997), in which multiple candidate models are simultaneously considered and the contribution from each model in explaining the data is scored following Bayes' theorem, aiming to increase the generalization ability of the Bayesian model. Therefore, we hereafter refer to the approach of Agata et al. (2021) as Bayesian multi-model fault slip estimation (BMMFSE). Thus, the BMMFSE is a generalized framework that considers the uncertainty of the underground structure in fault slip estimation. Although the advantages of using BMMFSE in fault slip inversion are discussed in detail in Agata et al. (2021), the method was only applied to a very simple numerical experiment. In the present study, we apply the method to estimate the slip distribution in SSEs, focusing on two advantages of BMMFSE.

### 1.2 Advantages of using BMMFSE for analyses of SSEs

One advantage is that BMMFSE allows for easier handling of the ill-posedness of slip estimation by introducing a fully Bayesian inference. In general, slip estimation is an ill-posed inverse problem, which is usually handled based on regularization by incorporating prior information on the characteristics of the slip distribution, such as smoothness and sparseness. The introduction of such information, which we hereafter call "strong prior" to distinguish it from weakly informative priors mentioned later, allows for obtaining a unique and stable solution by minimizing an objective function. Fully Bayesian inference is another approach to handle ill-posedness, which was recently introduced to fault slip estimation (e.g., Fukuda and Johnson (2008, 2010)): An ensemble of the solutions sampled from the posterior PDF is obtained in combination with weakly informative prior information for slip distribution, such as uniform distribution for the slip amount in each fault patch (e.g., Minson et al. (2013)). However, slip estimation using such weakly informative prior PDFs for slip distribution is prone to suffer more severely from overfitting to data errors. To avoid overfitting, accurately considering the model prediction errors originating from the uncertainty of the underground structure, which is often a major component of data errors (Duputel et al., 2014), by introducing BMMFSE is expected to be effective. Performing slip estimation based only on weakly informative prior PDFs has the potential to enable a more careful investigation of the spatial relationships between the estimated slip distribution of SSEs and hypocenter locations of the surrounding events: An investigation on the correspondence between the estimated slip distribution in SSEs and synchronized tremor hypocenters in the Cascadia subduction zone suggest that incorporation of strong prior constraints for slip distribution, such as spatial and temporal smoothing constraints, significantly affects the conclusion (Bartlow et al., 2011). In addition, a fused lasso method (Tibshirani et al., 2005), which promotes both sparsity and smoothness of the parameter distribution using L1-norm-based penalization, has also been applied to L-SSEs occurring beneath the Bungo Channel and found to be more effective for detecting discontinuous boundaries of the fault slip than using a widely used smoothing constraint based on a finite-difference approximation of the Laplacian operator (Nakata et al., 2017). This finding reconfirms the effect of the choice of regularization scheme on the estimation results of slip distribution.

The other advantage is that BMMFSE obtains the posterior PDF of the underground structure parameters in addition to those for the slip distribution. This means that the posterior PDF for the underground structure obtained in the analysis can be plugged into another estimation as the prior PDF. Such a method may be useful for further reducing the model prediction errors and validating the posterior PDF of the underground structure model obtained for each event. The estimation of SSEs occurring repeatedly at the same location can be a good application example of such a sequential estimation updating the underground structure.

### 1.3 Objectives

In this study, we estimate the posterior PDFs of the slip distribution of L-SSEs using BMMFSE, taking into account the uncertainty of the underground structure model by introducing many candidate models. We target L-SSEs that occurred beneath the Bungo Channel, southwest Japan, because of three features of these events: an increase in the number of deep tectonic tremors accompanying the L-SSEs was observed at the down-dip side of the main rupture area; multiple types of strong prior constraints have been applied to estimate past events; they occur repeatedly every six to eight years in almost the same location. These are the typical features of SSE for which BMMFSE may be advantageous, as explained in the last paragraph. For this purpose, we constructed a multi (ensemble) model to describe the uncertainty of the underground structure around the rupture area based on the database of the elastic structure and geometry of the plate boundary defined for southwest Japan and introduced it to the fully Bayesian inference of slip distribution. Thus, we estimated the posterior PDF for the slip distribution in the L-SSE that occurred around 2010 and 2018 using weakly informative prior PDFs. We compared the up- and down-dip limits of the slip distribution estimated based on BMMFSE and strong prior constraints in examining the spatial relationship with synchronized slow earthquakes in the surrounding regions. We also demonstrate a sequential estimation of the L-SSEs updating the underground structure by estimating the slip distribution in the 2018 L-SSE based on multiple models that describe the posterior PDF of the underground structure obtained in the estimation for the 2010 L-SSE. We examine the validity of the approach using an information criterion.

## 2 Observation data

The occurrence of L-SSEs beneath the Bungo Channel in southwest Japan, well known because of the continuous observation by the Global Navigation Satellite System (GNSS) conducted by the GNSS Earth Observation Network System (GEONET) (Miyazaki & Hatanaka, 1998) and managed by the Geospatial Information Authority of Japan, was observed repeatedly around 1997, 2003, 2010, and 2018. The main rupture areas of these four events are estimated to nearly coincide (Yoshioka et al., 2015; Ozawa et al., 2020; Seshimo & Yoshioka, 2021), filling a spatial gap between the deep ETS and seismogenic zones (Figure 1). Activities of deep tectonic tremors at the down-dip side and shallow very-low-frequency earthquakes (VLFEs) in the south of the main rupture area have shown rapid increases simultaneously with the acceleration phase of the L-SSEs (Hirose et al., 2010). Recent developments in data analysis techniques for GNSS data suggest that these major L-SSEs are accompanied by minor events of a smaller seismic moment release, which occurs nearly in the middle of the periods between the major events (Takagi et al., 2019). In this study, we focus on two recent major L-SSEs in this region that occurred around 2010 and 2018.

We used digital data for the observed vertical and horizontal displacements of the 2010 and 2018 L-SSEs (Figure 2), the former of which were provided by Yoshioka et al. (2015). The data for the latter were newly processed by Seshimo and Yoshioka (2021) based on the same approach of data analysis as that used in Yoshioka et al. (2015). The data were processed from the crustal displacements observed by GEONET. In all, we used 106 and 96 continuous GNSS stations in the estimation for the 2010 and 2018 events, respectively (some stations are excluded from the estimation for the latter event to avoid contaminating the displacement data with post-seismic deformation due to the 2016 Kumamoto earthquake following Seshimo and Yoshioka (2021)). We used only the total displacement of each component during periods from 2009.5 to 2011.2 and 2018.9 to 2019.5 in the decimal form, respectively. The dataset used for the 2010 L-SSE is identical to that used for the analyses of the same event in Nakata et al. (2017). We focused only on the spatial distribution to estimate the detailed distribution of the total slips during each L-SSE.

## 3 Estimation of the posterior PDF for the slip distribution considering the uncertainty of the underground structure

### 3.1 Formulation

We provide a summary of the formulation of BMMFSE, a method to estimate the posterior PDF for the slip distribution considering the uncertainty of the underground structure proposed by Agata et al. (2021). Let us consider an estimation problem of $\mathbf{m}$, which is a vector for the parameters of the slip distribution, from $\mathbf{d}$, a vector for the observation data. A widely used Bayesian formulation for estimating the posterior PDF for slip distribution, where a single underground structure model is chosen a priori, is written as follows:

$$P(\mathbf{m}|\mathbf{d}) \quad = \quad \kappa P(\mathbf{d}|\mathbf{m}) P(\mathbf{m}), \tag{1}$$

where $P(\mathbf{m}|\mathbf{d})$, $P(\mathbf{d}|\mathbf{m})$, and $P(\mathbf{m})$ are the posterior PDF of the slip parameters, the likelihood function, and the prior PDF of the slip parameters, respectively. $\kappa = 1/P(\mathbf{d})$ is a normalization factor that takes a constant value because the observation data and model are fixed. However, it is natural to assume that the probabilistic density for the model prediction described by $P(\mathbf{d}|\mathbf{m})$ also depends on the choice of the underground structure model, which we hereafter characterize using parameters $\boldsymbol{\varphi}$. This dependence can be incorporated in the likelihood function as $P(\mathbf{d}|\mathbf{m}, \boldsymbol{\varphi})$. Let us suppose that we know the PDF $P(\boldsymbol{\varphi})$ to describe the stochastic property of the uncertainty of the underground structure. Then, a posterior PDF for $\mathbf{m}$ considering the uncertainty of $\boldsymbol{\varphi}$ can be obtained by replacing the original likelihood function with $P(\mathbf{d}|\mathbf{m}, \boldsymbol{\varphi})$ and marginalizing the right-hand side with $\boldsymbol{\varphi}$, as

$$\begin{aligned} P(\mathbf{m}|\mathbf{d}) &= \int P(\mathbf{m}, \boldsymbol{\varphi}|\mathbf{d}) d\boldsymbol{\varphi}, && (2) \\ &= \kappa \int P(\mathbf{d}|\mathbf{m}, \boldsymbol{\varphi}) P(\mathbf{m}|\boldsymbol{\varphi}) P(\boldsymbol{\varphi}) d\boldsymbol{\varphi}. && (3) \end{aligned}$$

The widely used approach described by Equation 1 corresponds to a case in which $\boldsymbol{\varphi}$ is fixed a priori in Equation 3, that is, $P(\boldsymbol{\varphi}) = \delta(\boldsymbol{\varphi} - \boldsymbol{\varphi}_{\mathrm{fix}})$, that is, a single model is chosen in the "first step" described in Section 1. Here, we consider a situation in which uncertain information of the underground structure is available in the form of an ensemble consisting of random samples $\boldsymbol{\varphi}^{(n)}$ drawn from $P(\boldsymbol{\varphi})$, where $n = 1, \ldots, N$, and $N$ are sufficiently large numbers. By using the samples, the integration on the right-hand side of Equation 3 can be approximately evaluated based on Monte Carlo integration as:

$$\begin{aligned} P(\mathbf{m}|\mathbf{d}) &= \kappa \int P(\mathbf{d}|\mathbf{m}, \boldsymbol{\varphi}) P(\mathbf{m}|\boldsymbol{\varphi}) P(\boldsymbol{\varphi}) d\boldsymbol{\varphi} && (4) \\ &\simeq \kappa \frac{1}{N} \sum_{n=1}^{N} P(\mathbf{d}|\mathbf{m}, \boldsymbol{\varphi}^{(n)}) P(\mathbf{m}|\boldsymbol{\varphi}^{(n)}). && (5) \end{aligned}$$

Providing the likelihood function $\mathbf{d}$, $P(\mathbf{d}|\mathbf{m}, \boldsymbol{\varphi})$ in the form of a parametric distribution allows for the explicit calculation of the density $P(\mathbf{m}|\mathbf{d})$ for a given $\mathbf{m}$. In this study, we assumed a simple Gaussian distribution for the likelihood function as follows:

$$P(\mathbf{d}|\mathbf{m}, \boldsymbol{\varphi}) = (2\pi)^{-N_{\mathrm{d}}/2} ||\mathbf{E}||^{-1/2} \exp[-\frac{1}{2}(\mathbf{d} - \mathbf{G}(\boldsymbol{\varphi})\mathbf{m})^{\mathrm{T}} \mathbf{E}^{-1} (\mathbf{d} - \mathbf{G}(\boldsymbol{\varphi})\mathbf{m})]., \quad (6)$$

where $N_{\mathrm{d}}$, $\mathbf{E}$, and $\mathbf{G}(\boldsymbol{\varphi})$ are the dimensions of the data vector, the covariance matrix that is determined based on the error characteristics of the observation instruments and data processing, and the response matrix that relates the slip parameters and the response in the observation stations calculated based on elasticity for the given $\boldsymbol{\varphi}$, respectively. Thus, we can draw random samples of $\mathbf{m}$ from the posterior PDF $P(\mathbf{m}|\mathbf{d})$ using sampling methods such as Markov chain Monte Carlo (MCMC) methods (e.g., Metropolis et al. (1953)). We use the replica-exchange Monte Carlo method (REMC; Swendsen and Wang (1986); Geyer (1991)), which is also known as parallel tempering, an acceleration method of MCMC sampling.

The formulation of BMMFSE presented so far is based on Bayes' theorem for the joint posterior PDF for $\mathbf{m}$ and $\boldsymbol{\varphi}$. Interestingly, the same formulation can be obtained from a different starting point, that is, considering the variability in the model prediction defined by the likelihood function in the conventional formulation presented in Equation 1, as

$$P(\mathbf{d}|\mathbf{m}) = \int P(\mathbf{d}|\mathbf{d}_{\mathrm{pred}}) P(\mathbf{d}_{\mathrm{pred}}|\mathbf{m}) d\mathbf{d}_{\mathrm{pred}}, \quad (7)$$

where $\mathbf{d}_{\mathrm{pred}}$ and $P(\mathbf{d}_{\mathrm{pred}}|\mathbf{m})$ denote the predicted response at the observation point and the stochastic property of the model prediction for a given $\mathbf{m}$, respectively. This marginalization (integration) for $\mathbf{d}_{\mathrm{pred}}$ can be approximately conducted by Monte Carlo integration, resulting in the same calculation as presented in Equation 5 (see Section 2 of Agata et al. (2021) for details). This alternative derivation essentially suggests that the BMMFSE corresponds to a generalization of the formulation of Duputel et al. (2014) to a non-Gaussian scheme.

Once we obtain the samples of $\mathbf{m}$ and the values of the likelihood function associated with the samples via MCMC sampling, we can also approximate the posterior PDF of $\boldsymbol{\varphi}$. By replacing the marginalization in Equation 2 with one based on $\mathbf{m}$

with further transformation, we obtain

$$P(\boldsymbol{\varphi}|\mathbf{d}) = \int P(\mathbf{m},\boldsymbol{\varphi}|\mathbf{d})d\mathbf{m}, \tag{8}$$

$$= \int P(\boldsymbol{\varphi}|\mathbf{m},\mathbf{d})P(\mathbf{m}|\mathbf{d})d\mathbf{m} \tag{9}$$

$$= \int \frac{P(\mathbf{d}|\mathbf{m},\boldsymbol{\varphi})P(\boldsymbol{\varphi}|\mathbf{m})}{\int P(\mathbf{d}|\mathbf{m},\boldsymbol{\varphi}')P(\boldsymbol{\varphi}'|\mathbf{m})d\boldsymbol{\varphi}'}P(\mathbf{m}|\mathbf{d})d\mathbf{m}, \tag{10}$$

where we use the relation $P(\boldsymbol{\varphi}|\mathbf{m},\mathbf{d}) = P(\mathbf{d}|\mathbf{m},\boldsymbol{\varphi})P(\boldsymbol{\varphi}|\mathbf{m})/P(\mathbf{d}|\mathbf{m})$ and $P(\mathbf{d}|\mathbf{m}) = \int P(\mathbf{d}|\mathbf{m},\boldsymbol{\varphi}')P(\boldsymbol{\varphi}'|\mathbf{m})d\boldsymbol{\varphi}'$ in the transformation of Equation 9 to 10. Suppose we have obtained $M$ samples from $P(\mathbf{m}|\mathbf{d})$ based on the REMC sampling, because we set $P(\boldsymbol{\varphi}|\mathbf{m}) = P(\boldsymbol{\varphi})$ in the present problem, we can rewrite the equation and approximate $P(\boldsymbol{\varphi}|\mathbf{d})$ based on the Monte Carlo integration as

$$P(\boldsymbol{\varphi}|\mathbf{d}) = \int \frac{P(\mathbf{d}|\mathbf{m},\boldsymbol{\varphi})P(\boldsymbol{\varphi})}{\int P(\mathbf{d}|\mathbf{m},\boldsymbol{\varphi}')P(\boldsymbol{\varphi}')d\boldsymbol{\varphi}'}P(\mathbf{m}|\mathbf{d})d\mathbf{m} \tag{11}$$

$$\simeq \frac{1}{M}\sum_{m=1}^{M} \frac{P(\mathbf{d}|\mathbf{m}^{(m)},\boldsymbol{\varphi})P(\boldsymbol{\varphi})}{\frac{1}{N}\sum_{n=1}^{N} P(\mathbf{d}|\mathbf{m}^{(m)},\boldsymbol{\varphi}^{(n)})}. \tag{12}$$

$P(\boldsymbol{\varphi})$ can be approximated using the same $N$ samples of $\boldsymbol{\varphi}$ as those used for the Monte Carlo integration in Equation 5 and others by, for example, an approximation based on the Monte Carlo method as follows:

$$\hat{P}(\boldsymbol{\varphi}) = \frac{1}{N}\sum_{n=1}^{N} \delta(\boldsymbol{\varphi} - \boldsymbol{\varphi}^{(n)}), \tag{13}$$

where $\delta(\boldsymbol{\varphi} - \boldsymbol{\varphi}^{(n)})$ is a delta function that satisfies

$$\delta(\mathbf{x}) = \mathbf{0} \quad (\mathbf{x} \neq \mathbf{0}), \tag{14}$$

and

$$\int_{\mathbf{S}} f(\mathbf{x})\delta(\mathbf{x}-\mathbf{x}^*)d\mathbf{x} = \begin{cases} f(\mathbf{x}^*) & (\mathbf{x}^* \in \mathbf{S}) \\ 0 & (\mathbf{x}^* \notin \mathbf{S}). \end{cases} \tag{15}$$

By substituting this term into $P(\boldsymbol{\varphi})$ in Equation 12, the marginal posterior PDF of $\boldsymbol{\varphi}$ can also be written based on the approximation by the Monte Carlo method as

$$\hat{P}(\boldsymbol{\varphi}|\mathbf{d}) = \frac{1}{N}\sum_{n=1}^{N} w^{(n)}\delta(\boldsymbol{\varphi} - \boldsymbol{\varphi}^{(n)}), \tag{16}$$

where

$$w^{(n)} = \frac{1}{M}\sum_{m=1}^{M} \frac{P(\mathbf{d}|\mathbf{m}^{(m)},\boldsymbol{\varphi}^{(n)})}{\frac{1}{N}\sum_{n'=1}^{N} P(\mathbf{d}|\mathbf{m}^{(m)},\boldsymbol{\varphi}^{(n')})}. \tag{17}$$

Because $P(\mathbf{d}|\mathbf{m}^{(m)},\boldsymbol{\varphi}^{(n)})$ is already calculated when REMC sampling for $P(\mathbf{m}|\mathbf{d})$ is performed, as shown in Equation 5, we can readily evaluate $w^{(n)}$.

The formulation presented here and used in the following applications is based on the simplest approximation of $P(\boldsymbol{\varphi})$ using the delta function without weights. Other forms of the approximation of $P(\boldsymbol{\varphi})$ are also applicable to the proposed approach. For example, importance weighting can be used to enhance the approximation based on the delta function (see Appendix A for details).

### 3.2 Multiple models to describe the uncertainty property of plate boundary geometry and elastic structure model

We consider the static linear elasticity to relate the fault slip underground to displacement on the surface based on a two-layered underground structure model consisting of a half-space and a layer above it, corresponding to the mantle and crust, respectively. The slips are located on a curved surface that models the plate boundary. We assume that $\boldsymbol{\varphi}$ consists of parameters for the plate boundary geometry and elastic parameters, namely, rigidity and Poisson's ratio, which are calculated from the seismic velocity and density structure. Provided that the underground structure model possesses a certain amount of uncertainty, we consider an ensemble of multiple models to describe the uncertain property by setting properly $P(\boldsymbol{\varphi})$ based on the published models, to avoid bias in the estimation because of an a priori selection of $\boldsymbol{\varphi}_{\text{fix}}$ and overfitting.

Several geometry models for the plate boundary, including the Nankai Trough region, have been published. Here, we consider three models: Iwasaki et al. (2015), Hayes et al. (2018), and Nakanishi et al. (2018), which are hereafter referred to as the Iwasaki, Slab2, and Nakanishi models, respectively (Figure 3). The Iwasaki model is mainly based on the hypocenter distribution for the geometry with longer wavelengths, refined by results from seismic tomography, receiver function analysis, and active source experiment. Slab2 focuses more on comprehensive modeling on a global scale. The Nakanishi model is based on more detailed seismic survey results in the shallower part, while the deeper part is based on seismicity. We consider an ensemble of multiple models for the plate boundary geometry, assuming that the true plate boundary geometry can be modelled sufficiently well by one of the models based on a weighted average of the depth of the three geometry models, that is, the plate boundary geometry in the $n$-th sample within the multiple models is calculated as

$$z^{(n)}(\mathbf{x}) = W^{(n)}_{\text{Iwasaki}} z_{\text{Iwasaki}}(\mathbf{x}) + W^{(n)}_{\text{Slab2}} z_{\text{Slab2}}(\mathbf{x}) + W^{(n)}_{\text{Nakanishi}} z_{\text{Nakanishi}}(\mathbf{x}), \tag{18}$$

where $z^{(n)}(\mathbf{x})$, $z_{\text{Iwasaki}}(\mathbf{x})$, $z_{\text{Slab2}}(\mathbf{x})$, and $z_{\text{Nakanishi}}(\mathbf{x})$ are the $z$ coordinates of the plate boundary geometry at the location $\mathbf{x}$ in the horizontal plane in the $n$-th sample, Iwasaki model, Slab2, and Nakanishi model, respectively. $W^{(n)}_{\text{Iwasaki}}$, $W^{(n)}_{\text{Slab2}}$, and $W^{(n)}_{\text{Nakanishi}}$ are the weights of the Iwasaki, Slab2, and Nakanishi models in the $n$-th sample, satisfying $W^{(n)}_{\text{Iwasaki}} + W^{(n)}_{\text{Slab2}} + W^{(n)}_{\text{Nakanishi}} = 1$. We assume that the stochastic property of these weights follows the Dirichlet distribution with $\alpha_i = 1\,(i = 1, \ldots, K)$, which corresponds to a uniform distribution over the $K-1$-dimensional simplex, where $K$ is the number of the plate boundary geometry model considered and currently $K = 3$. Figure 4 shows a ternary plot to denote the samples from the prior PDF for the plate boundary geometry model when the ensemble size $N$ is taken to be 2,000.

It is difficult to uniquely choose the material properties of the crust and mantle for the two-layered model based on published detailed elastic structure models for the target domain. Here, we assume that this room for the choice of parameters is the source of uncertainty in the underground elastic property model. We constructed a crustal model based on the Japan Integrated Velocity Structure Model (JIVSM) database (Koketsu et al., 2009, 2012). The JIVSM contains a digital elevation model for a layered seismic velocity and density structure for the region beneath the Japanese Islands, including the P-wave velocity, S-wave velocity, and density of each layer. To create an ensemble of multiple models of the crust, we focus on the structure above the Moho at the hanging wall in a region between 130.8°E and 133.6°N in the east-west direction and 32.0°N and 34.4°N in the north-south direction, within which the observation points used for the estimation for the 2010 event are located. The random samples that consist of the ensemble to model the uncertainty of the crustal parameters are generated in the following manner, shown as two-dimensional schematics in Figure 5 (a). We randomly select $N$ grid points in the horizontal plane from the domain. Then, we focus on the one-dimensional structure below each point and use the crustal thickness and the average elastic parameters within the crust (the layers above the Moho) as the property of the sampling point. Thus, $N$ samples for the thickness and elastic parameters of the crust are obtained. For the properties of the mantle, we used the P-wave velocity structure model of Nakanishi et al. (2018), which includes more detailed information for spatial distribution, although only P-wave velocity is included in the database. In the same manner, as for the crustal model, the average P-wave velocity from the Moho to the bottom of their model, 60 km depth, below a randomly chosen grid point is considered as the elastic property for a sampling point (Figure 5 (b)). The corresponding S-wave velocity and density are set based on an empirical relation of the elastic parameters in the earth (Brocher, 2005). Figure 6 shows the histogram for the random samples of elastic parameters that describes the prior PDF when the ensemble size $N$ is taken to be 2,000. Because we focus only on static deformation, only two elastic parameters, rigidity and Poisson's ratio for the crust and mantle, denoted by $\mu^{(n)}_{\text{crust}}$, $\nu^{(n)}_{\text{crust}}$, $\mu^{(n)}_{\text{mantle}}$, and $\nu^{(n)}_{\text{mantle}}$, respectively, are explicitly used in the analyses.

In total, the $n$-th sample of the vector for the underground structure parameter consists of eight elements:

$$\boldsymbol{\varphi}^{(n)} = \{W^{(n)}_{\text{Iwasaki}}\, W^{(n)}_{\text{Slab2}}\, W^{(n)}_{\text{Nakanishi}}\, D^{(n)}_{\text{crust}}\, \mu^{(n)}_{\text{crust}}\, \nu^{(n)}_{\text{crust}}\, \mu^{(n)}_{\text{mantle}}\, \nu^{(n)}_{\text{mantle}}\}, \tag{19}$$

where $D^{(n)}_{\text{crust}}$ is the crustal thickness of the $n$ th sample. Note that some of the components in $\boldsymbol{\varphi}^{(n)}$ are not necessarily independent of each other. Table 1 shows a summary of the random samples for the underground structure.

Because it is natural to assume that the underground structure around the target region does not change drastically over several years, which is a typical interval between the two sequential L-SSEs, the posterior PDF of the underground structure obtained for the 2010 L-SSE can be used as input information for the estimation of the 2018 L-SSE as the prior PDF: Following the formulations in Section 3.1, we obtain the posterior PDF $P(\boldsymbol{\varphi}|\mathbf{d})$, which consists of the same multiple models as in the prior, while the importance weight $w^{(n)}$ on each member is updated through the slip estimation for the 2010 L-SSE. $P(\boldsymbol{\varphi}|\mathbf{d})$ that we obtain here can be used as $P(\boldsymbol{\varphi})$ in Equation 3. However, the weight of many members is likely close to zero through the estimation for the 2010 event, which may lead to failure in effectively approximating the posterior PDF in the next estimation. This is a problem known as "degeneracy", which is common to ensemble-based filtering methods such as the particle filter (Gordon et al., 1993; Kitagawa, 1993, 1996). We can use the same solution as deployed in the particle filter method, that is, resampling new multiple models from the weighted samples that consist of the posterior PDF of $\boldsymbol{\varphi}$ obtained in the previous estimation to approximate the prior PDF for the next estimation. Here, we use the most basic approach proposed in Kitagawa (1993), which performs sampling with replacement from the original samples with probabilities proportional to $w^{(n)}$.

### 3.3 Fault slip parametrization and calculation method

We consider a fault slip distribution at the plate boundary between 131.5°E and 133.5°E in the east-west direction, 32.15°N, and 33.9°N in the north-south direction and within the depth range of 0-55 km in the Nakanishi model. We expanded the slip distribution using a bilinear interpolation function. In parametrizing the slip distribution, we fix the horizontal position of the grid points that discretize the slip while considering a variety of geometric models of the plate boundary. Therefore, the depth and area of each small fault vary depending on the geometry of the model. The size of the grid spacing is an important parameter because it determines the number of unknown parameters in the estimation. A proper choice of the number of unknown parameters is another important factor in preventing overfitting, in addition to accurate consideration of model prediction errors. For most of the cases presented in the following section, a grid size of 16 km interval is used (Figure 7), determined based on the widely applicable Bayesian information criterion (WBIC) (Watanabe, 2013). WBIC approximates the Bayes free energy, or the minus logarithm of Bayes marginal likelihood, which plays an important role in a statistical model evaluation for singular statistical models (see the text in Supporting Information for details). We estimate the slip norm in each of the 130 small faults and a single rake deviation from the direction opposite to subduction, which is common to all small faults. The direction opposite to subduction is assumed to be 125° in the north-based azimuth following Heki and Miyazaki (2001). We also consider a hyperparameter $\sigma$ regarding the scaling of the observation errors, that is, we introduce a covariance matrix $\mathbf{E} = \sigma\mathbf{E}'$ into Equation 6, where the diagonal and non-diagonal components of $\mathbf{E}'$ are taken based on the knowledge of the property of observation errors and taken to be zero, respectively. The total number of elements in $\mathbf{m}$ in the case of a 16 km grid interval is 132.

The prior PDFs for the unknown parameters are based on a uniform distribution, which we regard as a typical weakly informative prior, as shown in Table 2. While the PDFs are essentially based on a uniform distribution, we use a cosine tapered uniform distribution for the prior PDF for slip distribution, which is characterized by four numbers $a', a, b, b'$, where $a' \leq a \leq b \leq b'$. The probability density is uniformly distributed in the range between $a$ and $b$, whereas the edge of the distribution is tapered using a cosine curve in the range between $a'$ and $a$, and $b$ and $b'$ (see Appendix B for details). Such tapered uniform distribution is often used when a high probability of a parameter is expected near the edge of the uniform distribution in the posterior PDF. An estimation of slip distribution can be a typical example of such a case. The prior PDF for non-negative constraint is often used, while it is natural to expect that the amount of slip in many of the small faults tends to be nearly zero. We use a cosine taper only for the lower edge of the distribution, in the range between -0.1 m and 0 m. The lower limit -0.1 m is chosen as a limit of back slip allowed based on the Nankai Trough subduction zone, in which the convergence rate is estimated to be around 0.06 m/year (Heki & Miyazaki, 2001). Since the target period for the processed GNSS date for the 2010 L-SSE is 1.7 years, 0.1 m ($\simeq$ 0.06 m/year $\times$ 1.7 years) is used as the lower limit. Although the target period for the 2018 L-SSE is shorter (0.6 years), the same prior PDF is used for this event for ease of comparison with the 2010 L-SSE.

2,000 sets of the response function to each of the input unit fault slip in the direction of subduction and one perpendicular to it are calculated using EDGRN/EDCMP (Wang et al., 2003). Each set corresponds to the matrix $\mathbf{G}(\boldsymbol{\varphi})$ in Equation 6. In each iteration of the REMC sampling, these response functions in the two directions are superimposed according to the slip norm in each fault and the common rake deviation given in $\mathbf{m}$ in the current sampling step.

To draw samples from the posterior PDF using the REMC method, we took replicas $L = 32$ (and 48 for some cases depending on the setting). We take 150,000 burn-in steps and 350,000 sampling steps. Replica exchange is performed once in every five steps between two randomly selected replicas. We output a sample in every 50 steps to avoid taking strongly correlated samples. Because the algorithm requires the calculation of $\mathbf{G}(\boldsymbol{\varphi})\mathbf{m}$ in Equation 6 for each $\boldsymbol{\varphi}^{(n)}$ at every time step, proper acceleration is necessary. We accelerate the sampling calculation using multi-GPGPU (i.e., general-purpose computing on graphics processing units), assigning a GPU to the calculation for every replica. The use of 16 NVIDIA A100 GPUs, installed in Earth Simulator 4 at Japan Agency for Marine-Earth Science and Technology (JAMSTEC), allows sampling to be completed within less than an hour.

### 3.4 Numerical experiment

We present numerical experiments in a problem setting that mimics the actual estimation problem described in the next section. We used artificial data calculated based on the true fault slip and underground structure and applied BMMFSE to the estimation of both the slip and the structure based on the prior PDF for the underground structure introduced in the previous subsections. We consider two true slip models, $\mathrm{SM}_{\mathrm{sharp}}$ and $\mathrm{SM}_{\mathrm{smooth}}$: The former exhibits a discontinuous change in the slip distribution, and the latter has a smooth distribution in the entire region (Figure 8 (a) and (d)). We investigate how BMMFSE and a conventional method, which is based on a single underground structure model and a strong prior constraint based on a discretized Laplacian operator to impose smoothness on the slip distribution (explained in detail later), estimate the slip distribution for the two models. The true underground structure model assumed here is given by the average of the two plate boundary geometry models, Slab2 and the Iwasaki model (i.e., $W_{\mathrm{Iwasaki}} = 0.5$, $W_{\mathrm{Slab2}} = 0.5$, and $W_{\mathrm{Nakanishi}} = 0$), and elastic parameters presented in Table 3. The response displacement is calculated based on these true models. We added artificial Gaussian noise to the calculated displacements, for which the standard deviations were $2 \times 10^{-3}$ m for the horizontal component and $6 \times 10^{-3}$ m for the vertical component, following the error level presented in Yoshioka et al. (2015). $\mathbf{E}'$ is obtained according to this standard deviation setting.

The estimated fault slips using BMMFSE are shown in Figure 8. The mean slip distribution ((b) for $\mathrm{SM}_{\mathrm{sharp}}$ and (e) for $\mathrm{SM}_{\mathrm{smooth}}$) implies that the proposed method can distinguish the tight and broad distributions in $\mathrm{SM}_{\mathrm{sharp}}$ and $\mathrm{SM}_{\mathrm{smooth}}$, respectively. However, because BMMFSE estimates non-Gaussian posterior PDFs, solely mean values are not sufficient. Figure 8 (c) and (f) shows frequency plot of slips in the MCMC samples along the A-B line marked in (a), (b), (d) and (e). Because the region with large slips, which spans from 60 to 120 km away from Point A, is mostly beneath the Bungo Channel and lacks observation stations above, estimation uncertainty is relatively large. On the other hand, the overall distribution of the estimated frequency was consistent with the true slip distribution in both models. Figure 9 shows the plots for the posterior PDF for the underground structure for the $\mathrm{SM}_{\mathrm{sharp}}$. For the parameters of the plate boundary geometry (Figure 9 (a) and (b)), $W_{\mathrm{Slab2}}$ is distributed around 0.5, and $W_{\mathrm{Iwasaki}}$ and $W_{\mathrm{Nakanishi}}$ have a similar distribution to that of each other, although the probability density near the point representing the true model appears to be slightly large. These findings suggest that the data cannot clearly distinguish the weights of the Iwasaki and Nakanishi models, while the true model is estimated to be nearly an average of Slab2 and a weighted average of the two models. This is reasonable because the Iwasaki and Nakanishi models are far closer to each other than Slab2, as shown in Figure 3. The estimation result for the plate boundary in $\mathrm{SM}_{\mathrm{smooth}}$ shows the same tendency (Figure S1). In the estimation of the elastic parameters (Figure 9 (c) and (d)), no strong peak is estimated in the bin for the true values in the histograms. In the crust, relatively strong peaks observed in the prior distribution disappear in the posterior distribution. It appears that the data are insensitive to the parameters for the mantle because the prior and posterior do not have significant differences.

For comparison, we also performed an estimation using a conventional method, including a certain amount of model prediction errors. We use the Nakanishi model for the plate boundary geometry assuming a homogeneous elastic half-space with $\nu = 0.25$, which is one of the most widely used settings of the elastic property in slip inversion using geodetic data. The conventional method we consider here uses a strong prior constraint based on a finite-difference approximation of the Laplacian operator for the smoothness of the slip distribution, which we hereafter call the "smoothing" model. The smoothing model is taken with a Bayesian model with a prior constraint on the smoothness with unknown hyperparameters, which is determined using an information criterion (Yabuki & Matsu'ura, 1992). The estimated slip distributions of $\mathrm{SM_{sharp}}$ and $\mathrm{SM_{smooth}}$ on the A-B line are shown in Figure 8 (c) and (f), respectively. Due to the smoothness constraints, relatively smooth distributions are obtained not only for $\mathrm{SM_{smooth}}$ but also for $\mathrm{SM_{sharp}}$. In particular, the slip distribution on the down-dip side of the channel (approximately 120 to 150 km from Point A), for which $\mathrm{SM_{sharp}}$ and $\mathrm{SM_{smooth}}$ have a steep and smooth variation, respectively, are estimated to be similar smooth variations for both models. Thus, the introduction of a smoothness constraint may lead to difficulty in distinguishing the sharpness of the slip distribution at the down-dip side of the channel, unlike the estimates using BMMFSE.

# 4 Posterior PDF of slip distribution and underground structure based on the geodetic data for the L-SSEs occurring beneath the Bungo Channel around 2010 and 2018

## 4.1 Posterior PDF for slip distribution

Figure 10 shows an overview of the posterior PDF for the slip distribution $P(\mathbf{m}|\mathbf{d})$ estimated for the 2010 L-SSE. The mean model of the posterior PDF of $\mathbf{m}$ is plotted in Figure 10 (a). The main rupture area with a mean slip larger than 0.1 m is estimated to occur in a relatively narrow region in the north-south direction. The mean of the predictive PDF for the displacement (see Appendix C for the definition of the predictive PDF) agrees well with the observation data (Figure 10 (b)(c)) and is not associated with a significant systematic residual distribution (Figure S2 (a)(b)). However, because the posterior PDF of $\mathbf{m}$ has a non-Gaussian feature, only paying attention to the mean model may be misleading in understanding the features of the posterior PDF. Figure 10 (d) shows the normalized frequency of sampled slip parameter on the line from A to B marked in (a) and the histograms of slips in selected small faults. The amount of slip in the dip direction in the region between approximately 60 km and 120 km from Point A (e.g., (ii) in Figure 10 (d)) , which corresponds to the area directly beneath the Bungo channel, has a large variation, while those elsewhere have significantly large frequencies around the bin of 0 m slip (e.g., (i) and (iii) in Figure 10 (d)). This contrast clearly reflects the effect of the absence of observation points in the channel. The rake deviation of the slip from the direction opposite to subduction (i.e., 125° in the north-based azimuth) in the counter-clockwise direction was estimated to be approximately five degrees with a standard deviation of approximately one degree, which corresponds to a slip direction of approximately 120° azimuth. These results are consistent with the slip direction estimated for the fault patches with large slip amounts by Yoshioka et al. (2015) (see Figure S3 and the text in Supporting Information).

The histograms of slips in (i), (ii), and (iii) show asymmetric distribution shapes. This non-Gaussian feature of the marginal posterior PDF for the estimated slip suggests that the use of standard deviation may be inappropriate for quantifying the estimation uncertainty. Instead, we calculate the information gain before the posterior marginal PDFs based on the following definition:

$$IG_i = \int_{-\infty}^{\infty} P(m_i|\mathbf{d}) \log_2 \frac{P(m_i|\mathbf{d})}{P(m_i)} dm_i, \tag{20}$$

where $IG_i$ and $m_i$ are the information gain, whose unit is bit here, and the slip amount in the $i$-th small fault, respectively. The PDF regarding $m_i$ here is marginalized. Information gain is also known as the Kullback-Leibler divergence, which quantifies the difference between two PDFs. The integration and density $P(m_i|\mathbf{d})$ in Equation 20 are evaluated approximately by using the Monte Carlo integration and kernel density estimation based on the REMC samples, respectively. Figure 10 (e) shows a plot of the information gain for each small fault via the estimation for the 2010 event. Information gain is relatively small, not only in the small faults at the northern and southernmost parts, which are distant from the locations of the observation points but also in those beneath the Bungo Channel, around which the largest mean slip is estimated.

We also calculated the PDF for the seismic moment release following the definition of the predictive PDF. Fault slip at small faults with a small information gain should not be considered when calculating the seismic moment release. Otherwise, the prior PDF for the slip amount, which is characterized by a uniform distribution between 0 and 1 m, may have a substantial impact and lead to a significant bias in seismic moment estimation, that is, the mean model of the prior PDF for slip results in a uniform slip of 0.5 m, which corresponds to nearly $M_w$ 8, an unrealistically large value for an L-SSE. Although there is no objective criterion for this information-gain threshold to calculate the seismic moment, the resulting seismic moment releases $M_o$ falls in the same order as those estimated in previous studies when $IG = 1.5$ is used as the information gain threshold, that is, $(2.74 \pm 0.57) \times 10^{19}$ N m, which corresponds to $M_w$ 6.89±0.06, where the number following ± corresponds to a 2-$\sigma$ value. $IG = 0$ results in significantly larger $M_o$ and $M_w$ than those estimated in previous studies (Table 4). Note that the mean and standard deviation values do not satisfy the relation of and $M_w$ because we calculated the statistics for $M_w$ based on the random samples, for each of which we converted $M_o$ to $M_w$ using the relation. In addition, it is not straightforward to perform a fair comparison of seismic moment release estimated by employing widely used approaches and a Bayesian estimation scheme based on a weakly informative prior, as indicated by the above discussion.

Figure 11 shows the overview of the posterior PDF for slip distribution $P(\mathbf{m}|\mathbf{d})$ in the 2018 L-SSE. The main rupture area of the mean slip distribution is seen in a similar location but with a relatively small amount of slip compared to that of the estimate for the 2010 event (Figure 11 (a)). As in the case of the 2010 L-SSE, the mean of the predictive PDF for the displacement agrees well with the observation data (Figure 11 (b)(c)). The systematic residual distribution is not significant except for the southern part of Kyushu Island (stations located at around 32°N) (Figure S2 (c)(d)), which is unlikely to have a significant impact on the estimation results for the main rupture area. Although there is a significant amount of uncertainty, the 2018 L-SSE is likely to have hosted a smaller moment release, for example, $(2.35 \pm 0.51) \times 10^{19}$ N m, which corresponds to $M_w$ 6.84±0.07, when $IG = 1.5$ is adopted. This relationship is reasonable because the event duration we focus on in this study was significantly shorter in the 2018 L-SSE. However, the normalized frequency of the sampled slip parameter on the cross line from A to B shows a similar feature to that in the 2010 event, suggesting that these events are similar in terms of the up- and down-dip limits of the slip distribution (Figure 11 (d)). Similar to the 2010 L-SSE, the rake deviation of the slip from the direction opposite to subduction (i.e., 125° in the north-based azimuth) was estimated to be approximately five degrees with a standard deviation of approximately one degree. As a result, the histogram for the slip direction estimated for the 2018 L-SSE shows a similar pattern to that of the one in 2010 (Figure S3).

### 4.2 Posterior PDF for underground structure

Figure 12 (b) shows the ternary plots for the posterior PDF for the plate boundary geometry models obtained in the estimation for the 2010 L-SSE. The small triangles corresponding to $0.3 \leq W_{\text{Slab2}} \leq 0.6$ have frequencies that are approximately five times higher at maximum than the average frequency in the ternary plot for the prior PDFs shown again in Figure 12 (a). This pattern indicates that the geodetic dataset prefers an intermediate plate boundary model between Slab2 and a mixture of the Iwasaki and Nakanishi models. On the other hand, these small triangles with a high frequency do not have strong contrast in terms of the values of $W_{\text{Iwasaki}}$ and $W_{\text{Nakanishi}}$, which suggests that the dataset does not clearly distinguish between the contributions of the Iwasaki and Nakanishi models, similar to the results of the numerical experiment presented in Section 3.4. In contrast, the histograms for the posterior PDF for the elastic structure do not change significantly from those for the prior, with an increase in frequency at a maximum of approximately twice in each bin of the histograms (Figure 13 (b)). These results are consistent with previous reports that the choice of plate boundary model often has a larger impact on the estimation results than that of the elastic structure in estimating slip distribution using geodetic data (e.g., Lindsey and Fialko (2013); Li and Barnhart (2020)).

The weighted samples visualized in Figure 12 (b) and Figure 13 (b) are resampled using the approach explained in Section 3.2 to generate the new ensembles of the underground structure models used as the input for the estimation of the 2018 L-SSE. The ternary plot and the histograms for the new samples (Figure S4) are almost identical to those presented in Figure 12 (b) and Figure 13 (b). Figure 12 (c) and 13 (c) show the ternary plots and the histogram for the posterior PDF for the plate boundary geometry and the elastic structure model, respectively, obtained in the estimation for the 2018 L-SSE. The basic feature in the obtained posterior PDFs is the same as in the estimation results for the 2010 L-SSE, with further higher frequencies in the triangles corresponding to $0.4 \leq W_{\text{Slab2}} \leq 0.6$ for the posterior PDF of the plate boundary geometry model.

# 5 Discussion

## 5.1 Comparison of up- and down-dip limit of slip distribution with methods based on stronger prior constraints

We compare the estimation results obtained by using BMMFSE with those obtained using two previous methods based on strong prior constraints. One is the smoothing model, which was also used in the numerical experiments in Section 3.4. The Nakanishi model and an elastic half-space with $\nu = 0.25$ were used as the plate boundary model and elastic structure, following the setting of the numerical experiments. The other is a fused lasso model, which is obtained by using a fused lasso method (Tibshirani et al., 2005), which promotes both sparsity and smoothness of the parameter distribution using L1-norm-based penalization. We use the result from Nakata et al. (2017), who applied this method to L-SSEs in the Bungo Channel aiming at detecting discontinuous changes in the slip distribution, as the fused lasso model. The fused lasso model is only available for the 2010 L-SSE and is also based on an elastic half-space with $\nu = 0.25$ but uses a different plate boundary geometry model based on Baba et al. (2002).

Figure 14 (a) and (c) show the comparison of slip estimation results for the 2010 and 2018 L-SSE obtained by using BMMFSE and the previous methods. The slip profile at the up-dip side of the main rupture area in the three models (denoted by the orange double-headed arrows in (a) and (c)) agrees well with each other in the 2010 L-SSE and the two models in the 2018 L-SSE. On the other hand, we found significant variations at the down-dip side. In the 2010 L-SSE, at the location where the slope of the slip distribution at the down-dip side starts (denoted by the cyan double-headed arrow only in (a)), while the mean models of BMMFSE and the fused lasso model agree well in terms of the slope, the smoothing model shows a slightly larger amount of slip than in the others. In the location further from A (denoted by the pink double-headed arrow in (a) and (c)), we observe a moderate slope in the slip distribution of the smoothing model in contrast to the steep one seen in BMMFSE. This feature of difference is even clearer in the 2018 L-SSE. We observed similar differences at the down-dip side in the comparison between the BMMFSE and the smoothing model in the numerical experiment presented in Section 3.4. Therefore, it is likely that this moderate slope in the smoothing model is an artifact introduced owing to the use of a strong prior constraint and an underground structure that is likely to have introduced a significant amount of model prediction errors. The fused lasso model exhibits a large amount of slip with a flat distribution shape owing to the L1-norm-based penalty on the smoothness in the area of the pink double arrows. The histograms of the slip amount on line (i) shown in Figure 10 (d) and 11 (d) estimated by BMMFSE in a patch within this down-dip region suggest that the posterior PDF indeed permits a larger amount of slip, but the probability for such cases is not very high, according to our analyses.

During the period of both L-SSEs, a number of deep tremors synchronously occurred at the down-dip side of the main rupture region (the white bars in Figure 14), the number of which increased compared to the period before the L-SSEs (see Figure S5 and note that the occurrence of surrounding S-SSEs reported by Kano et al. (2019) is considered when counting the number of tremors). Although there seems to be a correspondence between the estimated slope of the slip distributions at the down-dip side and the distribution of the number of tremors, further discussion is difficult if only based on this information. Therefore, we calculate the change in the Coulomb failure stress ($\Delta$CFS) because of the estimated slip during the L-SSE period using an analytical expression of elastic deformation in a homogeneous half-space (Comninou & Dundurs, 1975). We use a simple form for calculating the change as

$$\Delta\mathrm{CFS} = \Delta\tau + f\Delta\sigma_{\mathrm{n}} \tag{21}$$

where $\Delta\tau$ is the shear stress change on the fault, $f$ is the effective friction coefficient, and $\Delta\sigma_{\mathrm{n}}$ is the normal stress change with the expanding direction as positive. The direction for shear stress is taken to be the opposite of the subduction. We only calculated $\Delta$CFS for the estimation results of BMMFSE and the smoothing model because the fused lasso model, which allows abrupt changes in the spatial distribution of the parameters, is not suitable for calculating the shear stress on the fault. Note that efforts have also been made to introduce a prior constraint that combines the distribution of smoother variations globally and abrupt changes locally in the framework of the fused lasso method (Nakata et al., 2016). We present the result assuming $f = 0.2$ for both models, reflecting an estimation result for a relatively low friction coefficient in the deep fault (Houston, 2015). For BMMFSE, the elastic half-space with Poisson's ratio of the elastic parameter of the mantle layer is used to calculate the shear and normal stresses.

Figure 14 (b) and (d) compare $\Delta$CFS calculated based on the slip distribution obtained using BMMFSE and that of the smoothing model for the 2010 and 2018 L-SSE, respectively. In both events, the location of the peak of the positive value of the mean $\Delta$CFS in the down-dip side of the channel for BMMFSE (denoted by the red star in (b) and (d)) is consistent with the bin with the largest number of tectonic tremors during the L-SSE period. On the other hand, the location of the corresponding peak in the smoothing model is not very consistent with that of the tremor distribution in the 2010 L-SSE, and such a peak with a positive $\Delta$CFS is insignificant in the 2018 L-SSE (denoted by the green star). Moreover, BMMFSE estimates a steeper slip distribution in the down-dip for the 2018 L-SSE, which results in a narrower region along the line for positive $\Delta$CFS, compared to those for the 2010 one (see the gray double-headed arrows in (b) and (d)). This contrast of the broad and narrow region of positive $\Delta$CFS appears to agree to the spatial change of tremors: the number of tremors during the 2018 L-SSE abruptly decreases from the first bin to the second bin from the side of Point A, which is in contrast to the more moderate decrease seen in the 2010 one. Such possible correspondences are blurred in the smoothing model. These contrasts between the two methods are observed robustly for different assumptions of $f$, indicated by the distribution of $\Delta\sigma_{\mathrm{n}}$ and $\Delta\tau$ (Figure S6), although we need to note that the uncertainty is that the calculated stresses are not small.

The correspondence between the spatial distribution of ΔCFS and tremors in the estimation results obtained using BMMFSE implies a direct mechanical relationship between slip in L-SSE and triggering of tremors. The mechanism of synchronization of L-SSE and tremors, which has also been observed in other subduction zones in the world, has remained controversial. For instance, for a similar synchronization known in the Guerrero subduction zone in Mexico, Kostoglodov et al. (2010) and Frank et al. (2015) attributed the synchronization to the increase in shear stress owing to L-SSE, while Villafuerte and Cruz-Atienza (2017) suggested that the stress concentration on the rupture front of the SSE owing to the increase in slip rate increased the number of tremors as the main mechanism. The results we obtain here seem consistent with the former mechanism. Of course, because we only focus on the total slip distribution during the L-SSE period, detailed discussion requires investigation of spatio-temporal evolution, such as that performed in Villafuerte and Cruz-Atienza (2017). Nevertheless, our results suggest that estimation of slip distribution with and without introducing strong prior constraints may lead to a qualitatively different conclusion on the synchronization of SSEs and surrounding slow earthquakes. For example, the slip distribution models adopted in the studies on L-SSEs in the Guerrero subduction zone referred to above were based on fault slip estimation using smoothing constraints. Therefore, the effects of these constraints on their discussion should be studied further. Bartlow et al. (2011) considered the relationship between S-SSE and tremors in the Cascadia subduction zone in North America, taking into consideration the impact of the smoothing filter in estimating the slip distribution of SSE suggested by numerical experiments. Fault slip estimation incorporating only weakly informative prior PDFs, as performed in this study, can be a more direct solution to the possible confusion brought about by adopting strong prior constraints.

### 5.2 Underground structure models preferred by the geodetic data

It is understandable to expect that either the Iwasaki or the Nakanishi model represents well the true plate boundary geometry in the target region because these two models were constructed based on the combination of more local information than that used in Slab2, in which global data were more emphasized. For instance, the Nakanishi model combines information from seismic surveys for shallower and microseismicity for the deeper portion of the plate boundary. However, as shown in Section 4.2 and Figure 12 (b) and (c), the posterior PDF for the plate boundary model we obtained has a large frequency for the intermediate models between Slab2 and the mixture of the others. The depth of Slab2 is significantly larger than that of the Iwasaki and Nakanishi models, while those of the latter two models are relatively similar in most parts of the target region, as shown in Figure 3. Therefore, the depth of the group of the plate boundary models preferred by the data in our estimation is generally larger than those in the Iwasaki and Nakanishi models. On the other hand, the estimated plate boundary geometry in this study has a certain amount of uncertainty; for example, the model with the weights denoted by the pink and magenta circles in Figure 12 (a), (b), and (c) is associated with equally high probability in both the estimation for the 2010 and 2018 L-SSE. The plot of the resulting plate boundary models compared with the original three models in Figure 12 (d) shows that the difference in the model denoted by the pink color is within a few kilometers from the Nakanishi model at a depth range of approximately 30 km, where a large portion of slip is likely to take place. In the deeper portion of the Nakanishi model, the top of the hypocenter locations determined by seismic tomography analyses was chosen as the trace of the plate boundary (Yamamoto et al., 2013). Therefore, this small difference may be within the uncertainty of hypocenter locations. We also should note that our evaluation does not apply to the entire domain of each fault geometry model because the geodetic data we used here contain the information of the geometry only within a small portion of the domain.

In the estimation for the 2010 L-SSE, the relatively tall bins seen in the histograms for prior PDF for the crustal thickness and elastic parameters become unnoticeable in the posterior PDF: Despite these characteristic priors, the data suggest that it is difficult to constrain the details of the crustal layer using the geodetic data. One of the possible reasons for the large uncertainty in the posterior PDF for the crustal model is that the data cannot resolve the slips in the shallow portion of the fault plane well, which should be more strongly related to the shallow layers. The portion of the fault plane in which relatively large slips are estimated tends to be located deeper than the lower limit of the crustal layer.

Both the results for the 2010 and 2018 L-SSE, the histogram for the posterior PDF of the elastic parameters in the mantle layer has the highest frequency in the bins at the lower bound, which are taller than in the prior PDF. This finding implies that the insertion of another layer corresponding to the lower crust, for which it is natural to assume smaller rigidity and larger Poisson's ratio than in the mantle layer, to the two-layered elastic structure is a possible improvement for the present model setting. However, this improvement is beyond the scope of this study, because we assume that the insertion of another layer does not significantly affect the estimation results for slip distribution.

### 5.3 Effect of updating underground structure through sequential estimation of L-SSE

In the estimation for the 2018 L-SSE, the posterior PDF of the underground structure obtained for the 2010 L-SSE was used as the prior PDF. To see how incorporating the PDF for the underground structure updated through the estimation for the 2010 L-SSE affects the results of the 2018 L-SSE, we show the estimation result for 2018 using the original prior PDF (Figure 4 and 6) directly in Figure 15. Comparing this with the results shown in Figure 11, we do not observe a significant difference in the slip distribution. We observed almost the same features in the posterior PDF for the underground structure. In general, the proper choice of prior PDFs contributes to the avoidance of overfitting in an estimation. The similarity between the result for the 2018 L-SSE with and without the PDF for the underground structure obtained for that of 2010 implies that the original prior PDF for the underground structure constructed based on the published databases is sufficient to avoid overfitting. However, the posterior PDF of the plate boundary geometry in the result based on the original prior PDF has a smoother distribution with less concentration of frequencies than in the result based on the prior PDF obtained from the 2010 L-SSE. Noting that the 2010 L-SSE is likely to have hosted a broader slip region with larger seismic moment release than the 2018 event, it is natural that more information on the plate boundary geometry is included in the prior PDF from the 2010 estimation, which contributed to the reduction of the uncertainty of the posterior PDF. In addition, combination with the results from the preceding L-SSEs (i.e., The events that occurred in around 1997 and 2003) may also increase the accuracy of the estimation, because the region with large slip amounts estimated in previous studies (e.g., Yoshioka et al. (2015)) are slightly different from each other.

WBIC of the two estimations for the 2018 L-SSE with and without the prior PDF based on that for the 2010 one are -1521.54 and -1519.14, respectively. The difference of logarithmic marginal likelihood that is larger than two corresponds to "decisive" evidence in favor of the former model (Kass & Raftery, 1995). These facts quantitatively support the idea that updating the underground structure in a sequential estimation of L-SSEs allows for a more preferable Bayesian inference.

### 5.4 Future perspectives

In this study, we targeted the L-SSE in the Bungo Channel because multiple types of strong prior constraints have been applied in previous studies. In addition, the feature of the L-SSE that the events with fault slip that are detectable by the GNSS observation have repeatedly occurred in the same location is another important reason. However, we expect that fault slip estimation using the BMMFSE also provides insightful results for ordinary earthquakes. Although we focused on the estimation using a weakly informative prior PDF for the slip distribution, the accurate consideration of model uncertainty that the method allows for should also be effective in estimations introducing strong prior PDFs. Moreover, by taking a fully Bayesian approach, the method can be flexibly combined with not only the widely used constraints such as the smoothing approach but also recently proposed sophisticated implicit (e.g., trans-dimensional inversion (Dettmer et al., 2014)) and explicit (e.g., von Karman regularization (Amey et al., 2018, 2019)) regularization schemes, which is expected to increase the quality of estimation. The probability models that were used to generate the ensemble of multiple models for the underground structure were constructed in a relatively ad hoc manner in this study. The construction of a multi-model ensemble focusing on the genuine estimation errors of underground structure models is an important task in future work.

## 6 Conclusion

We estimated the slip distribution in the L-SSEs that occurred beneath the Bungo Channel in southwest Japan in around 2010 and 2018 using BMMFSE, a Bayesian multi-model fault slip estimation method. We performed the estimations using only weakly informative prior PDFs, such as uniform distribution instead of strong priors, by taking advantage of the accurate consideration of the model uncertainty for underground structures in BMMFSE. We use the term "strong priors" here to denote prior information on the characteristic of the slip distribution, such as smoothness, sparseness, and so on, which is incorporated to regularize the inverse problem. We constructed an ensemble of multiple models that represent the model uncertainty of underground structures as a combination of the mixture of currently published plate boundary geometry models (i.e., the Iwasaki model, Slab2, and the Nakanishi model) and two-layered elastic media based on published databases of a 3D elastic structure. The posterior PDF estimated for both the 2010 and 2018 L-SSEs presents a large probability for slip models with a narrow area for the main rupture along the line in the north-south direction. Compared with the estimation results obtained by using the previous methods based on strong prior constraints, we found significant differences in the fault slip profiles at the down-dip side of the main rupture area immediately beneath the Bungo Channel. A comparison of the Coulomb failure stress change ($\Delta$CFS) calculated based on the estimated slip distribution suggests that the spatial distribution of the area with positive $\Delta$CFS agrees better with that of deep tectonic tremors that synchronously occurred during the period of the L-SSE. Moreover, the difference of the shape of the area with positive $\Delta$CFS in for the 2010 and 2018 L-SSE calculated in BMMFSE may correspond to the contrast of the spatial distribution of the number of tremors that occurred in each event. The other advantage of BMMFSE, which should match the estimation for L-SSE, is that it can renew the posterior PDF of the underground structure through the estimation for each event. The posterior PDF for the underground structure estimated for the 2010 L-SSE suggests that the geodetic data prefer intermediate models between Slab2 and a mixture of the Iwasaki and Nakanishi models, and the data cannot distinguish the latter two models clearly. On the other hand, we did not find a strong preference for any of the multiple models of elastic structure through the estimation. The choice of the plate boundary geometry model likely is one of the main factors that cause model prediction errors. In the estimation for the 2018 L-SSE, the posterior PDF of the underground structure obtained for the 2010 one was used as the prior PDF. Such treatment results in a more precise estimation of the plate boundary geometry than in an estimation using the same prior PDF of underground structure as used in the estimation for 2010. A comparison of these two estimations with different prior PDFs in terms of an information criterion also suggests that the estimation using the renewed prior PDF results in a more preferable Bayesian inference.

**Table 1.** An example of a set of random samples for the underground structure consisting of 2,000 members. $n$ is the index of the samples. The units of $D$ and $\mu$ are km and GPa, respectively.

| $n$ | Plate boundary geometry | Elastic structure |
|---|---|---|
| 1 | 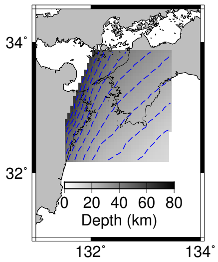 | $D_{\text{crust}}^{(1)}=32.7$<br>$\mu_{\text{crust}}^{(1)}=33.8$<br>$\nu_{\text{crust}}^{(1)}=0.235$<br>$\mu_{\text{mantle}}^{(1)}=63.2$<br>$\nu_{\text{mantle}}^{(1)}=0.258$ |
| ⋮ | ⋮ | ⋮ |
| 401 | 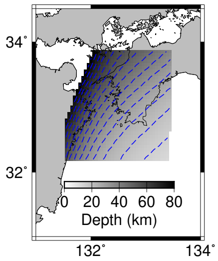 | $D_{\text{crust}}^{(401)}=31.7$<br>$\mu_{\text{crust}}^{(401)}=34.4$<br>$\nu_{\text{crust}}^{(401)}=0.235$<br>$\mu_{\text{mantle}}^{(401)}=60.7$<br>$\nu_{\text{mantle}}^{(401)}=0.260$ |
| ⋮ | ⋮ | ⋮ |
| 2,000 | 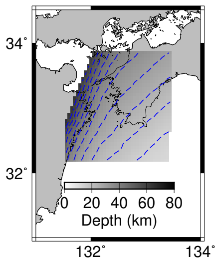 | $D_{\text{crust}}^{(2,000)}=36.2$<br>$\mu_{\text{crust}}^{(2,000)}=34.9$<br>$\nu_{\text{crust}}^{(2,000)}=0.234$<br>$\mu_{\text{mantle}}^{(2,000)}=56.1$<br>$\nu_{\text{mantle}}^{(2,000)}=0.262$ |

**Table 2.** The prior PDF for the unknown parameters. $U_{\cos}(a', a, b, b')$ denotes a cosine tapered uniform distribution, where the probability density is uniformly distributed in the range between $a$ and $b$, while the edge of the distribution is tapered using a cosine curve in the range between $a'$ and $a$, and $b$ and $b'$ (see Appendix B for details). $U(a, b)$ denotes a uniform probability distribution from $a$ to $b$, where $a < b$. $b_\sigma$ is a sufficiently large value, which is set to three in our computation program.

| | Slip norm | Rake deviation | Scale factor for observation errors |
|---|---|---|---|
| Prior PDF | $s_i \sim U_{\cos}$(-0.1 m, 0 m, 1 m, 1 m) | $\Delta\lambda \sim U$(-20°, 20°) | $\sigma \sim U(1, b_\sigma)$ |

**Table 3.** Elastic parameters for the true underground structure model assumed in the numerical experiments.

| $D_{\text{crust}}$ (km) | $\mu_{\text{crust}}$ (GPa) | $\nu_{\text{crust}}$ | $\mu_{\text{mantle}}$ (GPa) | $\nu_{\text{mantle}}$ |
|---|---|---|---|---|
| 23.0 | 31.2 | 0.238 | 62.0 | 0.258 |

**Table 4.** Seismic moment release ($M_o$) and corresponding moment magnitude ($M_w$) for estimated slip distribution in this study and previous ones. Note that the mean and standard deviation values do not satisfy the relation of $M_o$ and $M_w$ because we calculated the statistics for $M_w$ based on the random samples, for each of which we converted $M_o$ to $M_w$ using the relation.

| | 2010 L-SSE | | | | 2018 L-SSE | |
|---|---|---|---|---|---|---|
| | This study | | Yoshioka et al. (2015) | Nakata et al. (2017) | This study | |
| $IG$ threshold | 0 | 1.5 | - | - | 0 | 1.5 |
| $M_o$ ($10^{19}$N m) | 6.98±0.69 | 2.74±0.57 | 2.2 | - | 5.82±0.52 | 2.35±0.51 |
| $M_w$ | 7.16±0.03 | 6.89±0.06 | 6.8 | 6.9 | 7.11±0.03 | 6.84±0.05 |

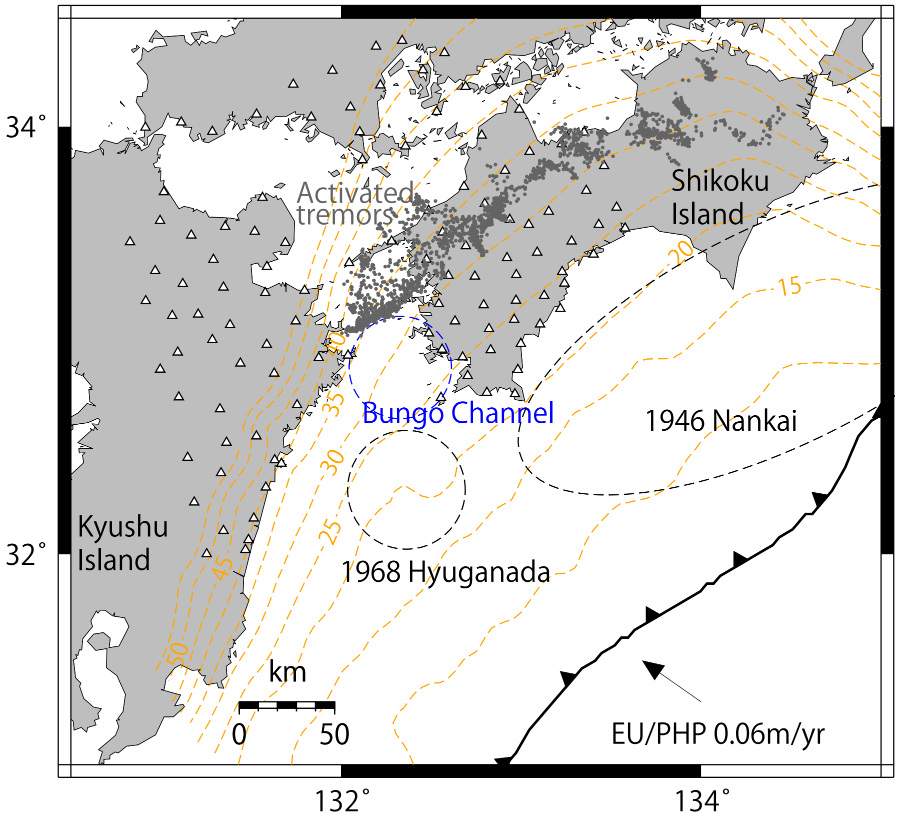


**Figure 1.** Tectonic setting for the target region. The blue dashed circle and the gray dots denote the location of the Bungo Channel and estimated hypocenters of tectonic tremors (Maeda & Obara, 2009; Obara, 2010; Kano et al., 2018) during the 2010 L-SSE. The ellipses with dashed lines indicate the approximate source areas of the 1946 Nankai and 1968 Hyuga-nada earthquakes. The orange dashed lines are the iso-depth contours drawn every five kilometers of the Nakanishi model as an example. The white triangles denote the locations of GEONET stations. The black arrow denotes the direction of the plate convergence rate between the Philippine Sea Plate and the Eurasian Plate.

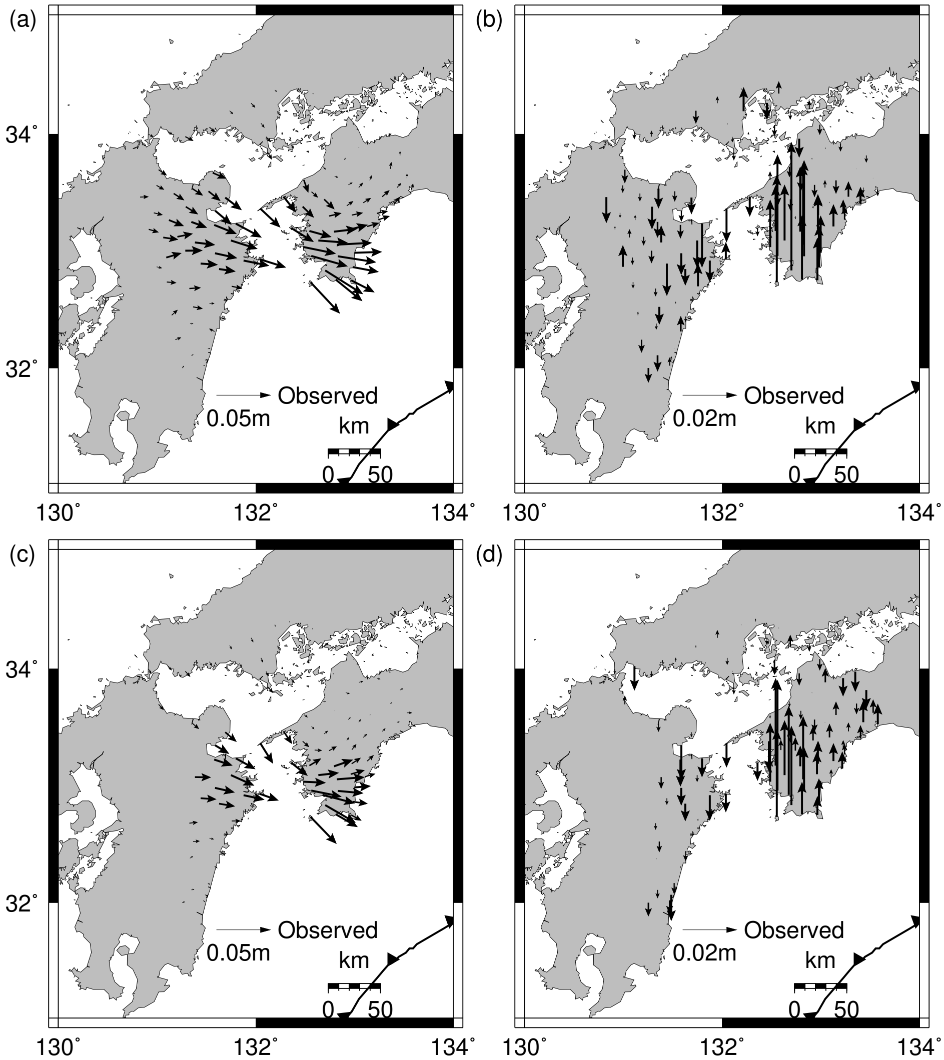


**Figure 2.** Surface displacement associated with the Bungo Channel L-SSE used in this study, derived from daily coordinates of GEONET (F3 solutions) by Yoshioka et al. (2015) and Seshimo and Yoshioka (2021). (a) Horizontal and (b) vertical displacements associated with the 2010 L-SSE. (c)(d) Those for the 2018 L-SSE.

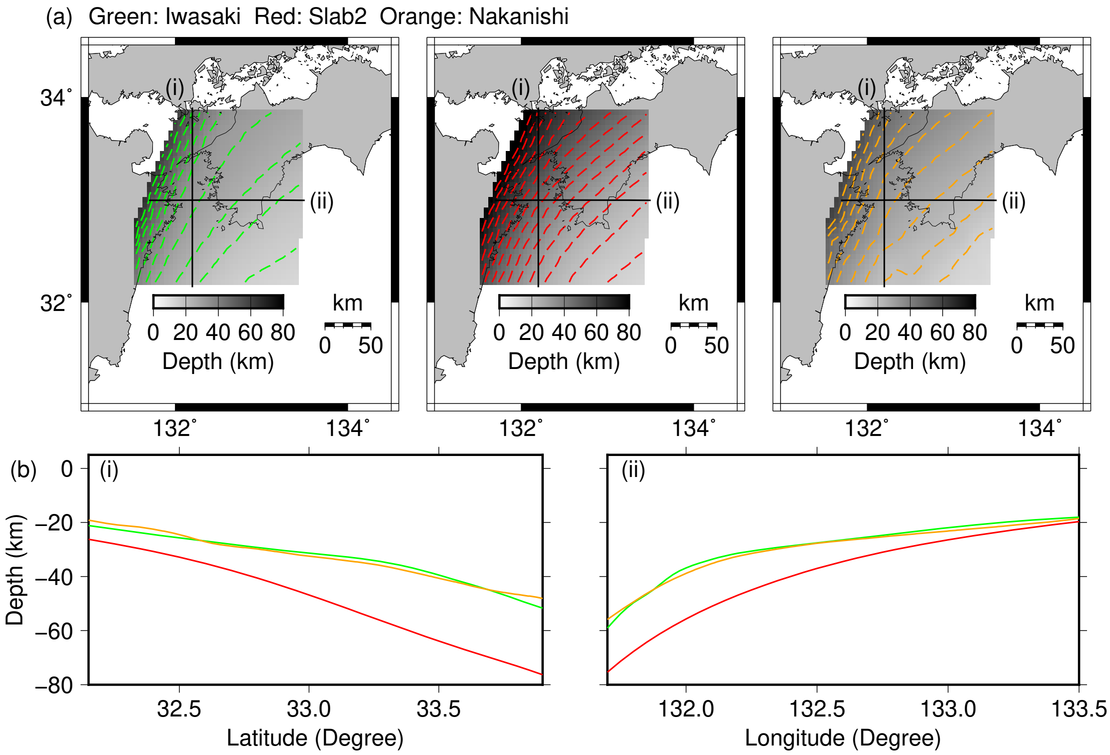


**Figure 3.** Comparison of three plate boundary geometry models, namely, the Iwasaki model, Slab2, and the Nakanishi model. (a) Plots of iso-depth contours for the three models. (b) Profiles on the lines denoted by (i) and (ii) in (a).

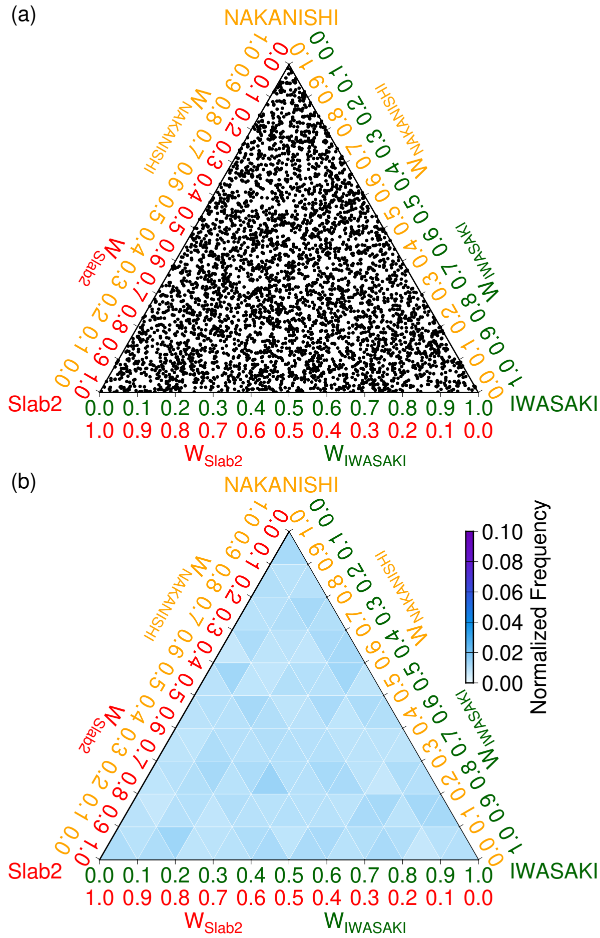


**Figure 4.** Ternary plots for the prior PDF for the plate boundary geometry model when the ensemble size $N$ is taken to be 2,000. (a) Plot of 2,000 samples using dots (b) Color map for the normalized frequency in each small triangle.

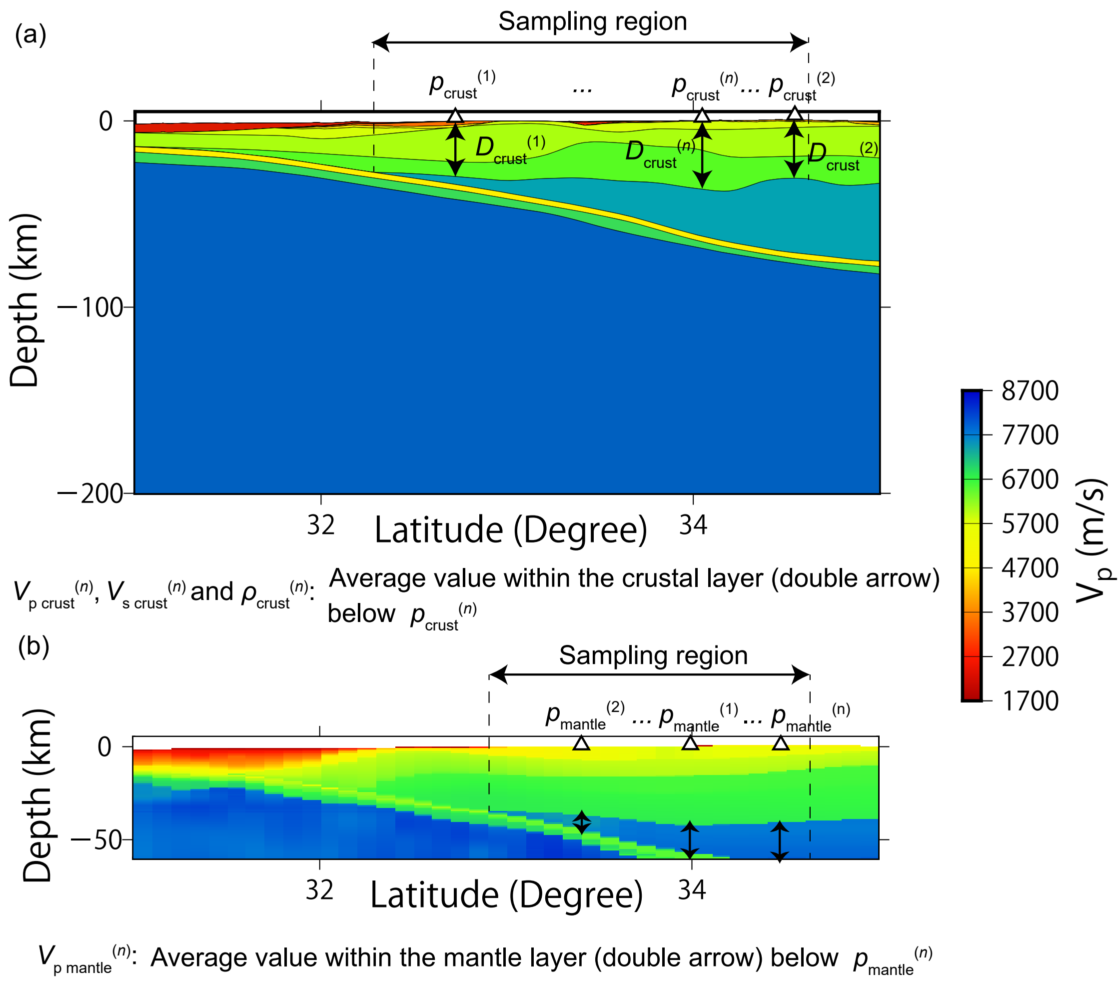


**Figure 5.** A two-dimensional schematic to explain the generation process of the random samples that consist of the ensemble to model the elastic structure with uncertainty. (a) Schematic of the samples of $D_{\mathrm{crust}}$, $V_{\mathrm{p\,crust}}$, $V_{\mathrm{s\,crust}}$, and $\rho_{\mathrm{crust}}$ based on JIVSM (Koketsu et al., 2009, 2012). (b) For $V_{\mathrm{p\,mantle}}$ based on the 3D P-wave velocity model of Nakanishi et al. (2018) ($V_{\mathrm{s\,mantle}}$ and $\rho_{\mathrm{mantle}}$ are calculated based on an empirical relationship with $V_{\mathrm{p\,mantle}}$).

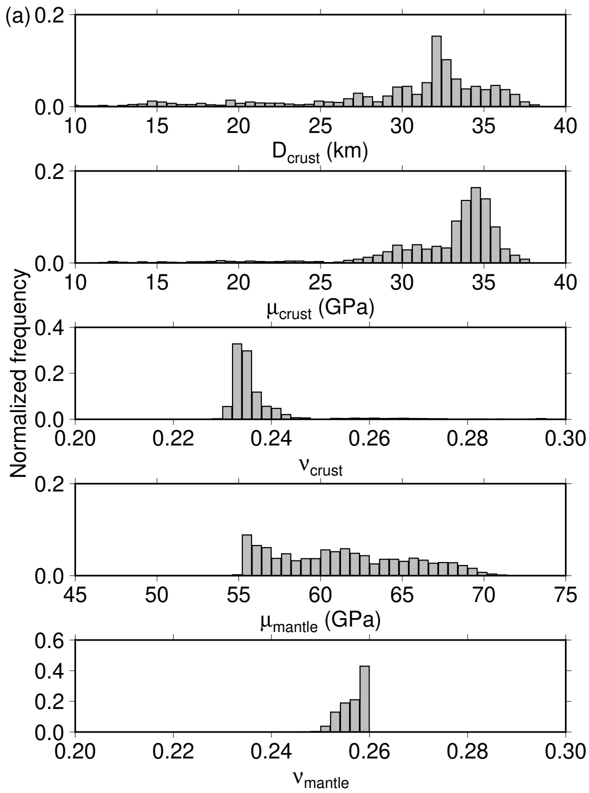


**Figure 6.** The histograms for the prior PDF of the elastic parameters when the ensemble size $N$ is taken to be 2,000.

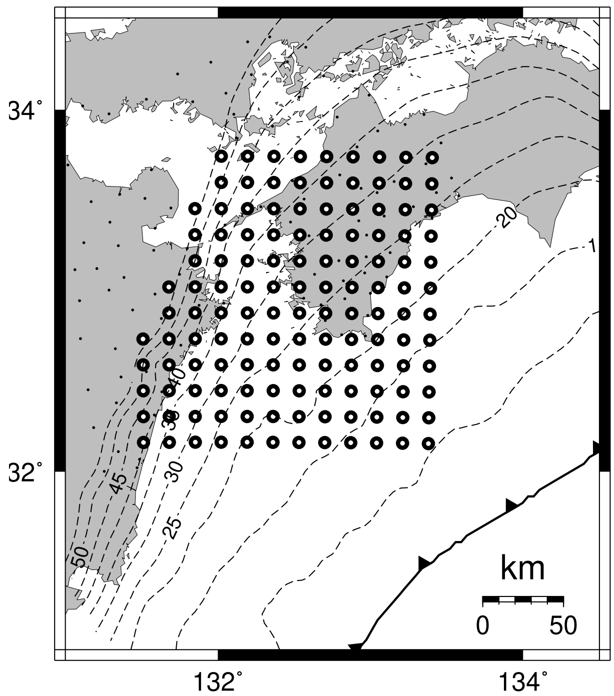


**Figure 7.** Configuration of slip parametrization. The black circles, dots, and dashed lines denote the central point of each small fault, the location of observation stations used in the 2010 estimation, and the iso-depth contour of the Nakanishi model as an example.

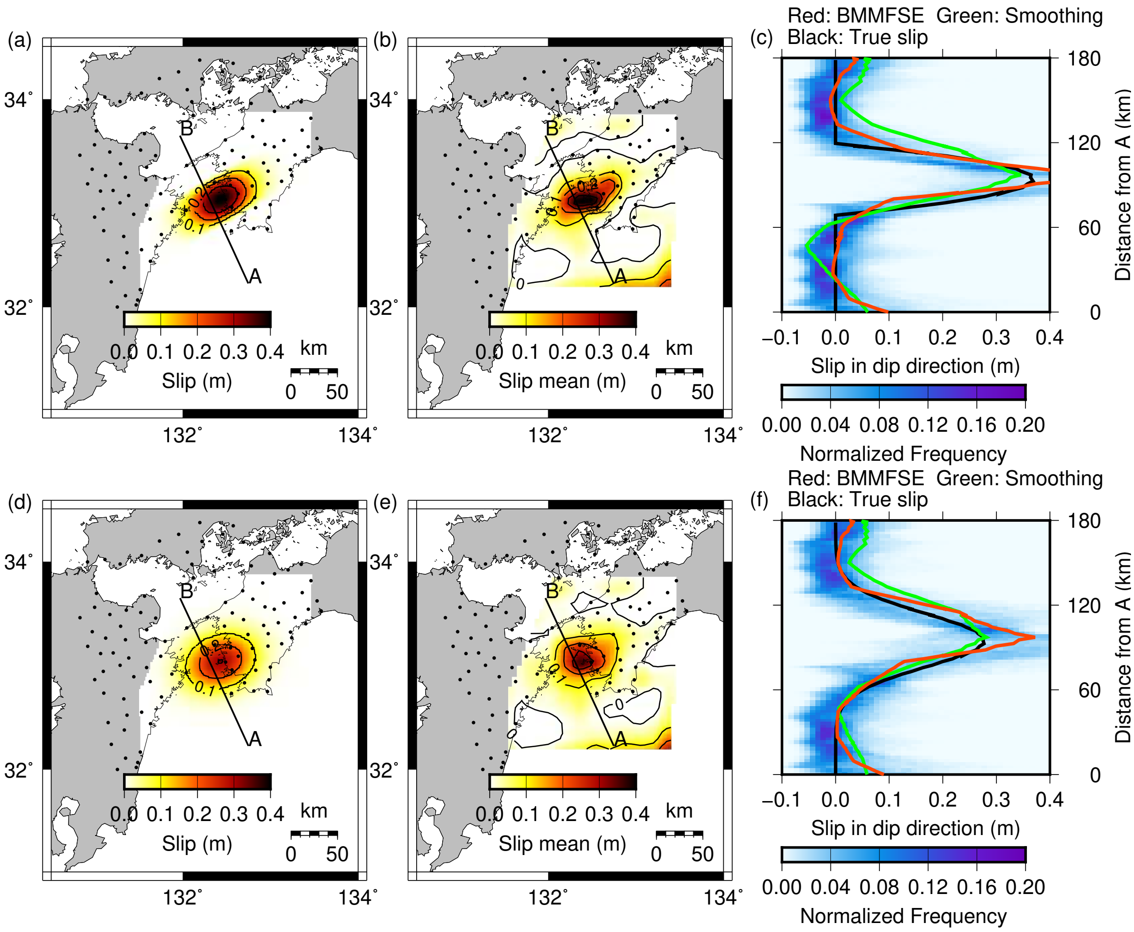


**Figure 8.** The estimation results for the numerical experiments. (a) True slip distribution of $SM_{sharp}$. (b) Mean model of the posterior PDF for the slip distribution estimated for $SM_{sharp}$ using BMMFSE. (c) Comparison of the slip distribution estimated using BMMFSE, the smoothing model, and the true slip distribution on the A-B line profile is denoted in (a) and (b). (d)-(f) Same as (a)–(c) but for $SM_{smooth}$.

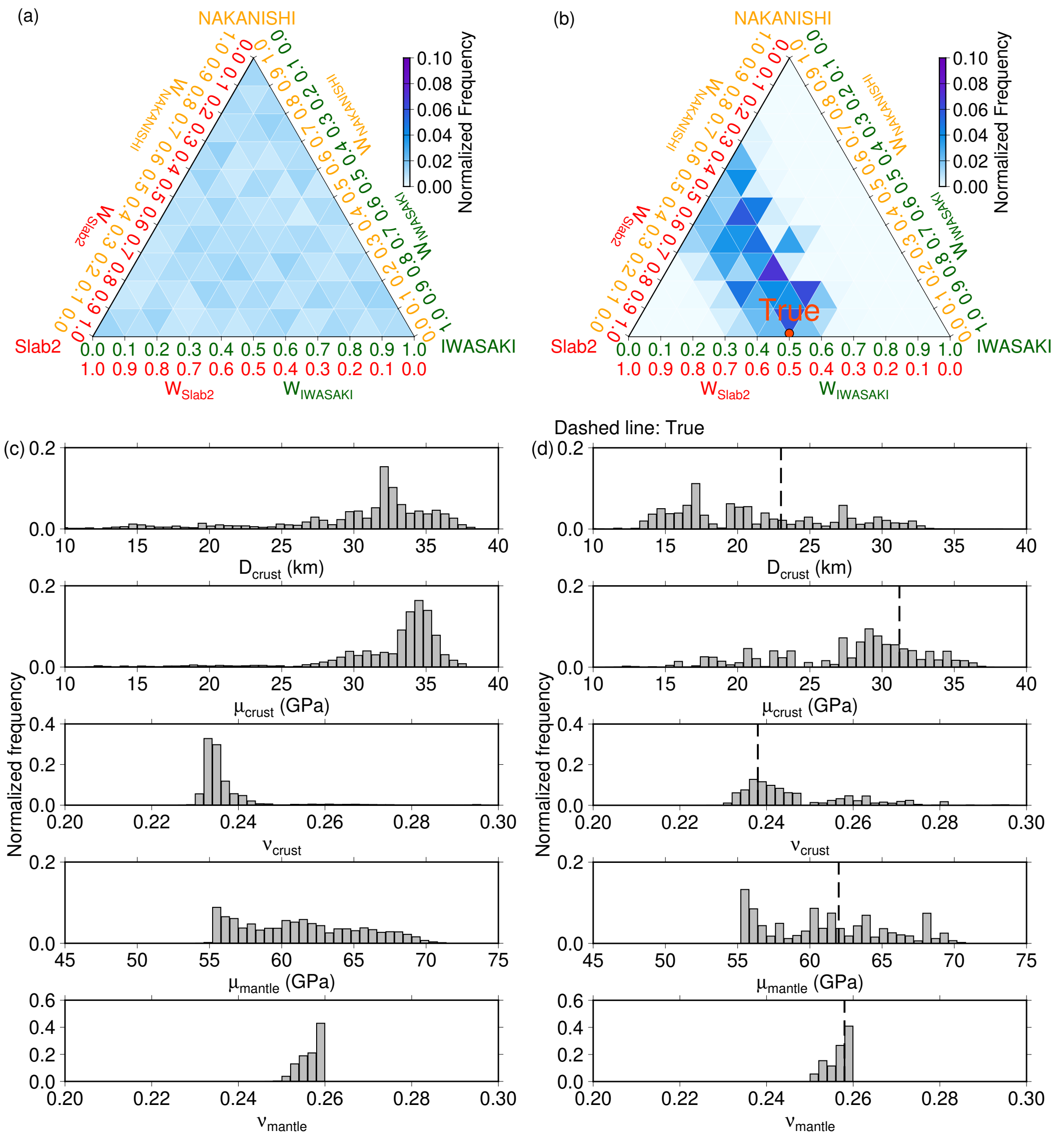


**Figure 9.** Comparison of the prior and posterior PDF of the underground structure in the numerical experiment for $SM_{sharp}$. Ternary plots for (a) the prior and (b) posterior PDFs of the plate boundary geometry model. Histograms illustrating (c) the prior and (d) posterior PDF of the elastic structure. (a) and (c) are identical to those in Figures 4 (b) and Figure 6.

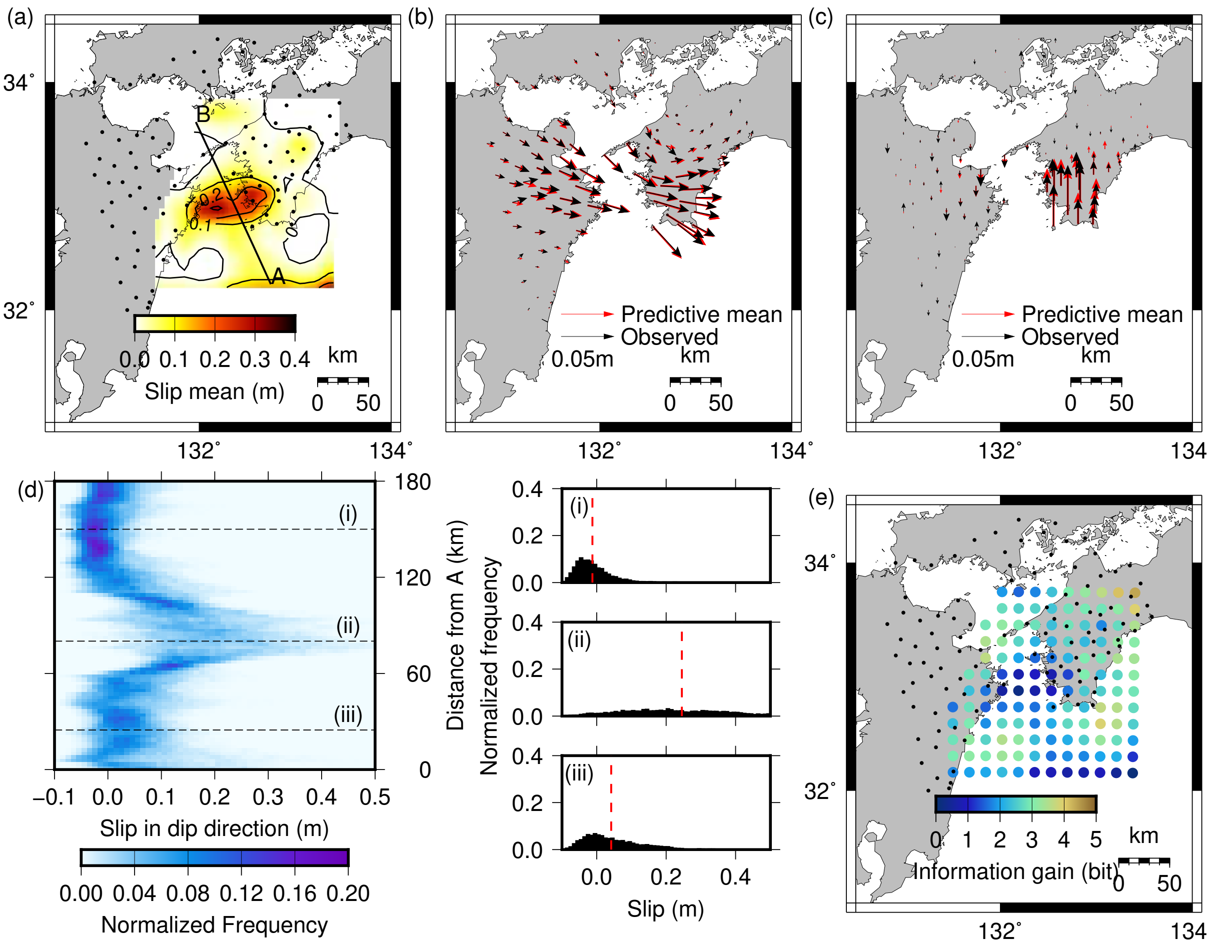


**Figure 10.** Estimation result of the slip distribution in the 2010 L-SSE obtained by using BMMFSE. (a) Mean model of posterior PDF for slip distribution. (b) Mean of the predictive PDF of and the observed horizontal displacement. (c) Vertical displacement (d) Color map of frequencies of amount of slip denoting the posterior PDF on the A-B line profile marked in (a) and the histograms in lines (i), (ii), and (iii) marked in the color map. The red dashed line denotes the mean values. (e) Information gain in Bayesian estimation for the 2010 L-SSE.

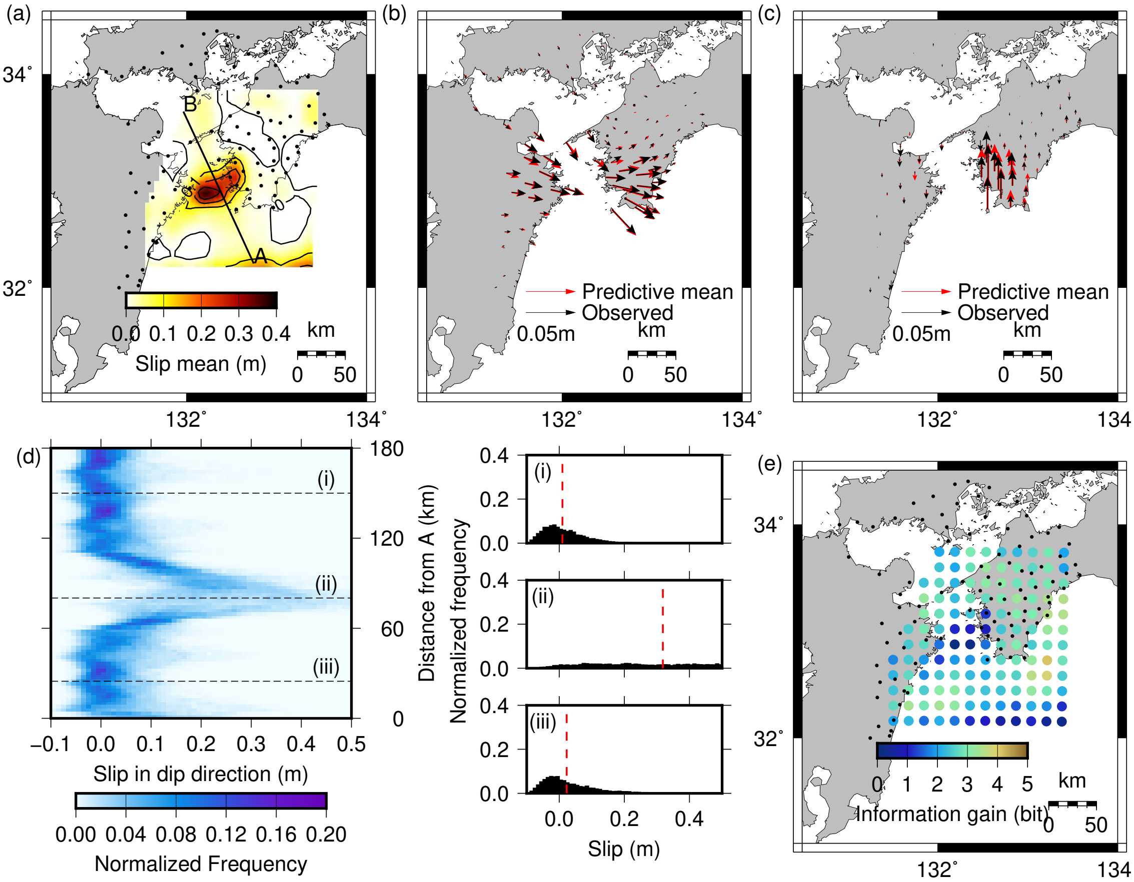


**Figure 11.** Estimation result of the slip distribution in the 2018 L-SSE obtained by using BMMFSE. (a) Mean model of posterior PDF for slip distribution. (b) Mean of the predictive PDF of and the observed horizontal displacement. (c) Vertical displacement (d) Color map of the frequencies of amount of slip denoting the posterior PDF on the A-B line profile marked in (a) and the histograms in lines (i), (ii), and (iii) marked in the color map. The red dashed line denotes the mean values. (e) Information gain in the Bayesian estimation for the 2018 L-SSE.

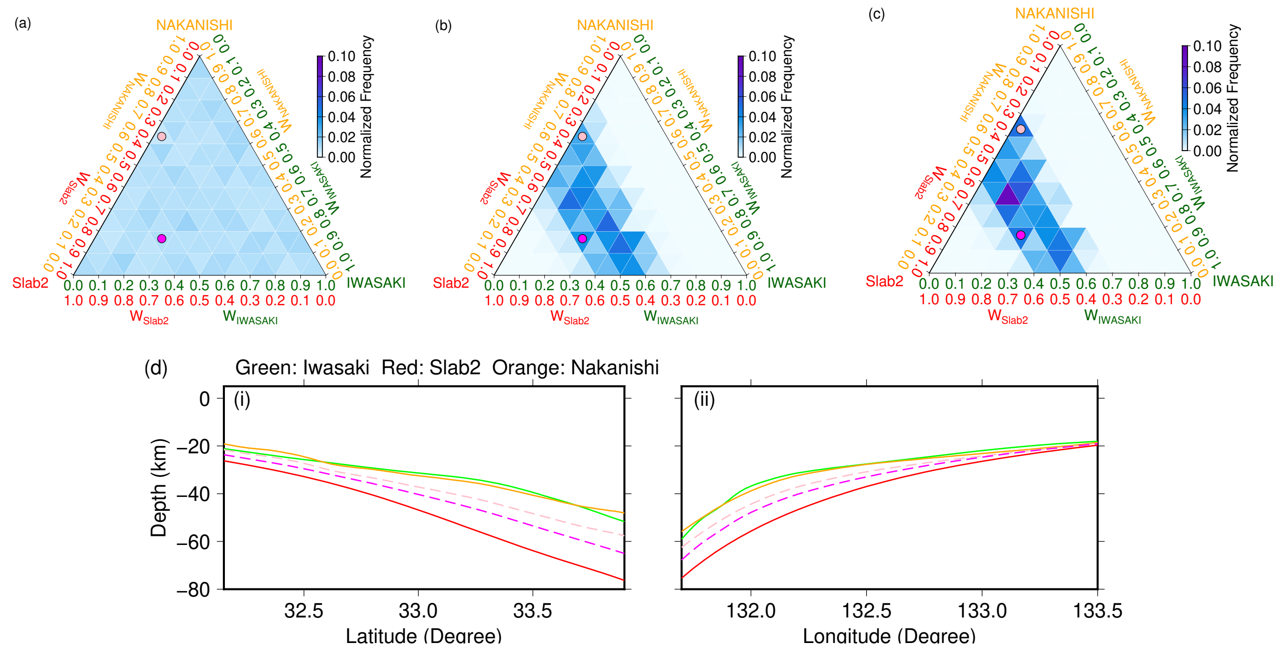

**Figure 12.** Comparison of ternary plots for the prior and posterior PDF of the plate boundary geometry model. (a) Prior PDF, which is identical to Figure 4 (b). (b) The posterior PDF obtained in the 2010 estimation. (c) For the 2018 estimation (d) Plate boundary geometries produced by the weights denoted by the locations marked by the pink and magenta circles in (a), (b), and (c), plotted in the same line profile shown in Figure 3.

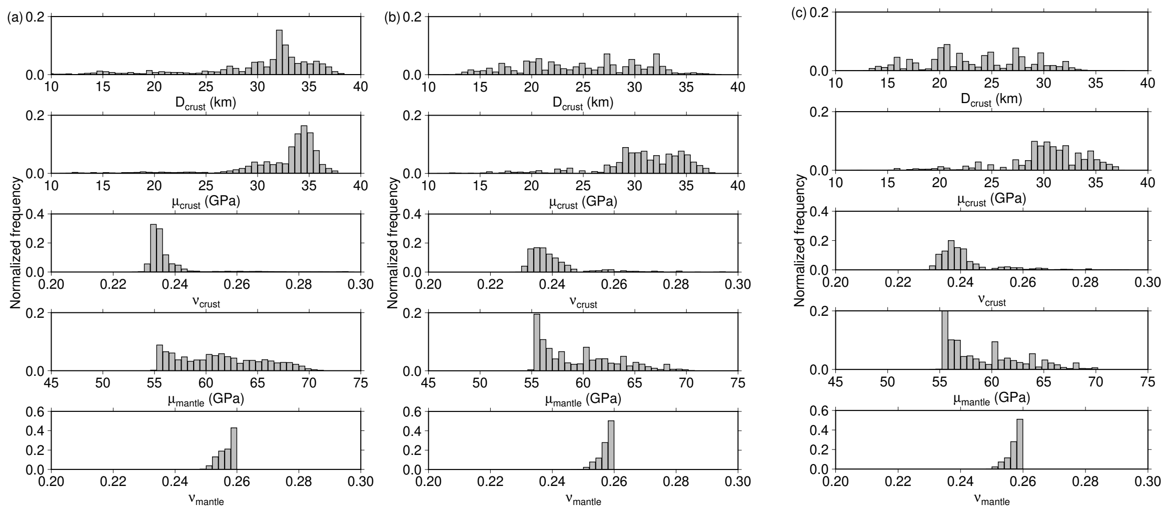

**Figure 13.** Comparison of the histogram plots for the prior and posterior PDF of the elastic parameters. (a) Prior PDF, which is identical to Figure 6. (b) The posterior PDF obtained in the 2010 estimation. (c) For 2018 L-SSE.

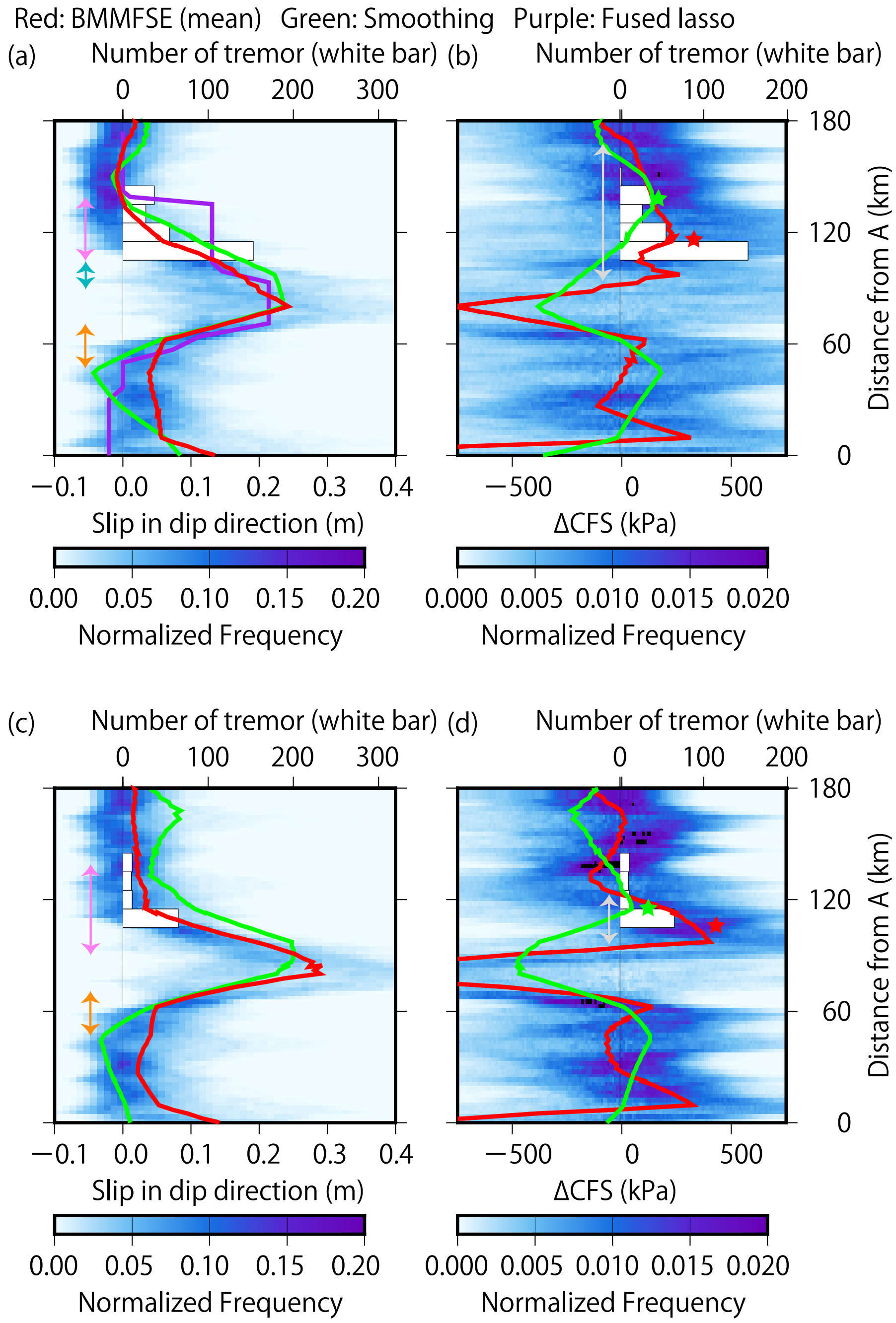


**Figure 14.** The correspondence between estimated slip distribution, ΔCFS and the tremor distribution on the A-B line profile. (a) Comparison of slip distribution models for 2010 L-SSE. The color map denotes the frequency of the amount of slip for the posterior PDF. The red, green, and purple lines denote the slip distribution of the mean of the BMMFSE, smoothing, and fused lasso models, respectively. (b) Comparison of the ΔCFS distributions for 2010 L-SSE. The color map denotes the frequencies of the ΔCFS values for the posterior PDF. The red and green lines denote the distribution of the mean of ΔCFS calculated based on the posterior PDF of the slip distribution estimated by BMMFSE and the ΔCFS distribution calculated based on the slip distribution of the smoothing model, respectively. The location of the peak of the positive value of the mean ΔCFS in the down-dip side of the channel for BMMFSE and the smoothing model are denoted by red and green stars, respectively. In all the figures, the white bars denote the number of tremors during the L-SSE period in the area within 5 km from the line in the direction perpendicular to it. (c)(d) Those for the 2018 L-SSE.

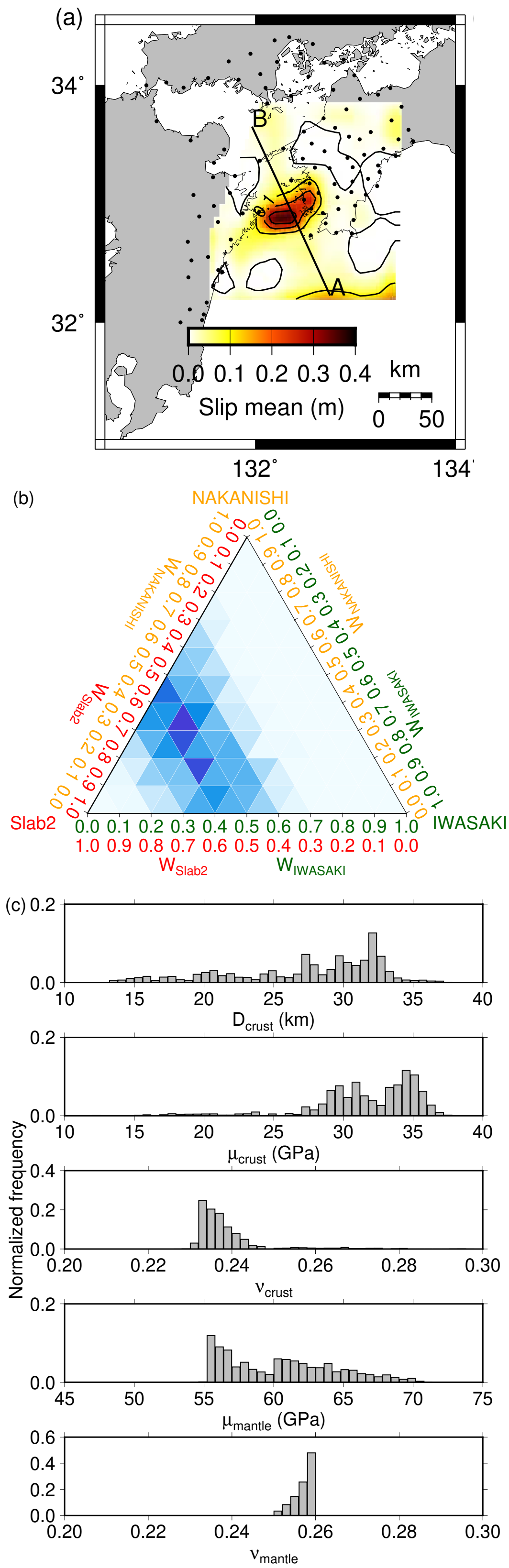


**Figure 15.** The estimation results for the 2018 L-SSE using the original prior PDF instead of the PDF for the underground structure updated through estimation for the 2010 one. (a) The mean slip distribution, the posterior PDF for (b) the plate boundary geometry and (c) the elastic structure.

## Appendix A Approximation of $P(\varphi)$ based on the particle approximation with importance weights

The formulation described in Section 3.1 is based on a simple particle approximation of $P(\boldsymbol{\varphi})$ as

$$P(\boldsymbol{\varphi}) \simeq \frac{1}{N}\sum_{n=1}^{N}\delta(\boldsymbol{\varphi}-\boldsymbol{\varphi}^{(n)}). \tag{A1}$$

The evaluation of the posterior PDF of $\mathbf{m}$ and $\boldsymbol{\varphi}$ is based on the particle approximation with importance weights, such as

$$P(\boldsymbol{\varphi}) \simeq \frac{1}{N}\sum_{n=1}^{N}g^{(n)}\delta(\boldsymbol{\varphi}-\boldsymbol{\varphi}^{(n)}), \tag{A2}$$

is also readily applicable as follows:

$$P(\mathbf{m}|\mathbf{d}) \simeq \kappa\frac{1}{N}\sum_{n=1}^{N}g^{(n)}P(\mathbf{d}|\mathbf{m},\boldsymbol{\varphi}^{(n)})P(\mathbf{m}|\boldsymbol{\varphi}^{(n)}) \tag{A3}$$

$$P(\boldsymbol{\varphi}|\mathbf{d}) \simeq \frac{1}{N}\sum_{n=1}^{N}g^{(n)}w^{(n)}\delta(\boldsymbol{\varphi}-\boldsymbol{\varphi}^{(n)}). \tag{A4}$$

## Appendix B The definition of the cosine tapered-uniform distribution

The PDF is for a cosine-tapered uniform distribution $U_{\cos}(a', a, b, b')$, and is defined as

$$P(x) = \kappa f(x), \tag{B1}$$

where

$$f(x) = \begin{cases} \frac{1}{2}\left(-\cos\left(\frac{x-a'}{a-a'}\pi\right)+1\right) & (a' \le x < a) \\ 1 & (a \le x \le b) \\ \frac{1}{2}\left(\cos\left(\frac{x-b}{b'-b}\pi\right)+1\right) & (b < x \le b') \\ 0 & (else) \end{cases} \tag{B2}$$

and $\kappa$ is the normalizing factor.

## Appendix C The definition and calculation of the posterior predictive PDF

The definition of the posterior predictive PDF for a certain physical quantity $\mathbf{x}$ (using a vector notation to maintain generality), for example, surface displacement, seismic moment release, and $\Delta$CFS as presented in the main text, based on the estimated Bayesian model is written as:

$$P(\mathbf{x}|\mathbf{D}) = \int\int P(\mathbf{x}|\mathbf{m},\boldsymbol{\varphi})P(\mathbf{m},\boldsymbol{\varphi}|\mathbf{D})d\mathbf{m}d\boldsymbol{\varphi}, \tag{C1}$$

where $P(\mathbf{m},\boldsymbol{\varphi}|\mathbf{D})$ is the joint posterior PDF of the model and the underground structure parameters obtained using the data $\mathbf{d} = \mathbf{D}$. After performing the REMC sampling, the double integration on the right-hand side of this equation is approximately evaluated as:

$$P(\mathbf{x}|\mathbf{D}) \simeq \frac{1}{M}\sum_{m=1}^{M}\int P(\mathbf{x}|\mathbf{m}^{(m)},\boldsymbol{\varphi})\frac{P(\mathbf{D}|\mathbf{m}^{(m)},\boldsymbol{\varphi})P(\boldsymbol{\varphi})}{\frac{1}{N}\sum_{n=1}^{N}P(\mathbf{D}|\mathbf{m}^{(m)},\boldsymbol{\varphi}^{(n)})}d\boldsymbol{\varphi} \tag{C2}$$

$$\simeq \frac{1}{NM}\sum_{n=1}^{N}\sum_{m=1}^{M}P(\mathbf{x}|\mathbf{m}^{(m)},\boldsymbol{\varphi}^{(n)})\frac{P(\mathbf{D}|\mathbf{m}^{(m)},\boldsymbol{\varphi}^{(n)})}{\frac{1}{N}\sum_{n'=1}^{N}P(\mathbf{D}|\mathbf{m}^{(m)},\boldsymbol{\varphi}^{(n')})}, \tag{C3}$$

where the value of $P(\mathbf{D}|\mathbf{m}^{(m)},\boldsymbol{\varphi}^{(n)})$ for each sample with the indices $m$ and $n$ is already available (see Equation 5 and the explanation therein).

## Acknowledgments

We appreciate the discussions on the plate boundary geometry model by Dr Ayako Nakanishi and Dr Yojiro Yamamoto. This research was supported by JSPS KAKENHI Grant Number JP16H06472 and JP19H04631 in Scientific Research on Innovative Areas "Science of Slow Earthquakes". The plate models by Iwasaki et al. (2015) were constructed from topography and bathymetry data by Geospatial Information Authority of Japan (250-m digital map), Japan Oceanographic Data Center (500m mesh bathemetry data, J-EGG500, `http://www.jodc.go.jp/jodcweb/JDOSS/infoJEGG_j.html`) and Geographic Information Network of Alaska, University of Alaska (Lindquist et al., 2004). This research was conducted using the Fujitsu PRIMERGY CX400M1/CX2550M5 (Oakbridge-CX) in the Information Technology Center, The University of Tokyo. Computational resources of the Earth Simulator 4 provided by JAMSTEC was also used.

## References

Agata, R., Ichimura, T., Hori, T., Hirahara, K., Hashimoto, C., & Hori, M. (2018). An adjoint-based simultaneous estimation method of the asthenosphere's viscosity and afterslip using a fast and scalable finite-element adjoint solver. *Geophysical Journal International*, *213*(1), 461-474. Retrieved from `http://dx.doi.org/10.1093/gji/ggx561` doi: 10.1093/gji/ggx561

Agata, R., Kasahara, A., & Yagi, Y. (2021). A bayesian inference framework for fault slip distributions based on ensemble modelling of the uncertainty of underground structure: with a focus on uncertain fault dip. *Geophysical Journal International*, *225*(2), 1392–1411.

Amey, R., Hooper, A., & Morishita, Y. (2019). Going to Any Lengths: Solving for Fault Size and Fractal Slip for the 2016, M w 6.2 Central Tottori Earthquake, Japan, Using a Transdimensional Inversion Scheme. *Journal of Geophysical Research: Solid Earth*, *124*(4), 4001–4016.

Amey, R., Hooper, A., & Walters, R. (2018). A Bayesian method for incorporating self-similarity into earthquake slip inversions. *Journal of Geophysical Research: Solid Earth*, *123*(7), 6052–6071.

Baba, T., Tanioka, Y., Cummins, P. R., & Uhira, K. (2002). The slip distribution of the 1946 Nankai earthquake estimated from tsunami inversion using a new plate model. *Physics of the Earth and Planetary Interiors*, *132*(1-3), 59–73.

Bartlow, N. M., Miyazaki, S., Bradley, A. M., & Segall, P. (2011). Space-time correlation of slip and tremor during the 2009 Cascadia slow slip event. *Geophysical Research Letters*, *38*(18).

Bartlow, N. M., Wallace, L. M., Beavan, R. J., Bannister, S., & Segall, P. (2014). Time-dependent modeling of slow slip events and associated seismicity and tremor at the Hikurangi subduction zone, New Zealand. *Journal of Geophysical Research: Solid Earth*, *119*(1), 734–753.

Brocher, T. M. (2005). Empirical relations between elastic wavespeeds and density in the Earth's crust. *Bulletin of the seismological Society of America*, *95*(6), 2081–2092.

Comninou, M., & Dundurs, J. (1975). The angular dislocation in a half space. *Journal of Elasticity*, *5*(3-4), 203–216.

Dettmer, J., Benavente, R., Cummins, P. R., & Sambridge, M. (2014). Transdimensional finite-fault inversion. *Geophysical Journal International*, *199*(2), 735–751.

Duputel, Z., Agram, P. S., Simons, M., Minson, S. E., & Beck, J. L. (2014). Accounting for prediction uncertainty when inferring subsurface fault slip. *Geophysical Journal International*, *197*(1), 464–482.

Frank, W. B., Shapiro, N. M., Husker, A. L., Kostoglodov, V., Bhat, H. S., & Campillo, M. (2015). Along-fault pore-pressure evolution during a slow-slip event in Guerrero, Mexico. *Earth and Planetary Science Letters*, *413*, 135–143.

Fukahata, Y., & Matsu'ura, M. (2006, jul). Quasi-static internal deformation due to a dislocation source in a multilayered elastic/viscoelastic half-space and an equivalence theorem. *Geophysical Journal International*, *166*(1), 418–434. Retrieved from `http://gji.oxfordjournals.org/cgi/doi/10.1111/j.1365-246X.2006.02921.x` doi: 10.1111/j.1365-246X.2006.02921.x

Fukahata, Y., & Wright, T. J. (2008). A non-linear geodetic data inversion using ABIC for slip distribution on a fault with an unknown dip angle. *Geophysical Journal International*, *173*(2), 353–364.

Fukuda, J., & Johnson, K. M. (2008). A fully bayesian inversion for spatial distribution of fault slip with objective smoothing. *Bulletin of the Seismological Society of America*, *98*(3), 1128–1146.

Fukuda, J., & Johnson, K. M. (2010). Mixed linear–non–linear inversion of crustal deformation data: Bayesian inference of model, weighting and regularization parameters. *Geophysical Journal International*, *181*(3), 1441–1458.

Geyer, C. J. (1991). Markov chain Monte Carlo maximum likelihood.

Gordon, N. J., Salmond, D. J., & Smith, A. F. (1993). Novel approach to nonlinear/non-Gaussian Bayesian state estimation. In *Iee proceedings f (radar and signal processing)* (Vol. 140, pp. 107–113).

Hayes, G. P., Moore, G. L., Portner, D. E., Hearne, M., Flamme, H., Furtney, M., & Smoczyk, G. M. (2018). Slab2, a comprehensive subduction zone geometry model. *Science*, *362*(6410), 58–61.

Heki, K., & Miyazaki, S. (2001). Plate convergence and long-term crustal deformation in central japan. *Geophysical Research Letters*, *28*(12), 2313–2316.

Hirose, H., Asano, Y., Obara, K., Kimura, T., Matsuzawa, T., Tanaka, S., & Maeda, T. (2010). Slow earthquakes linked along dip in the Nankai subduction zone. *Science*, *330*(6010), 1502–1502.

Hirose, H., & Kimura, T. (2020). Slip distributions of short-Term slow slip events in Shikoku, southwest Japan, from 2001 to 2019 based on tilt change measurements. *Journal of Geophysical Research: Solid Earth*, *125*(6), e2020JB019601.

Hirose, H., Matsuzawa, T., Kimura, T., & Kimura, H. (2014). The Boso slow slip events in 2007 and 2011 as a driving process for the accompanying earthquake swarm. *Geophysical Research Letters*, *41*(8), 2778–2785.

Houston, H. (2015). Low friction and fault weakening revealed by rising sensitivity of tremor to tidal stress. *Nature Geoscience*, *8*(5), 409–415.

Iwasaki, T., Sato, H., Ishiyama, T., Shinohara, M., & Hashima, A. (2015). Fundamental structure model of island arcs and subducted plates in and around japan. In *Agu fall meeting abstracts* (Vol. 2015, pp. T31B–2878).

Kano, M., Aso, N., Matsuzawa, T., Ide, S., Annoura, S., Arai, R., … others (2018). Development of a slow earthquake database. *Seismological Research Letters*, *89*(4), 1566–1575.

Kano, M., Kato, A., & Obara, K. (2019). Episodic tremor and slip silently invades strongly locked megathrust in the Nankai Trough. *Scientific reports*, *9*(1), 1–8.

Kass, R. E., & Raftery, A. E. (1995). Bayes factors. *Journal of the american statistical association*, *90*(430), 773–795.

Kitagawa, G. (1993). A Monte Carlo filtering and smoothing method for non-Gaussian nonlinear state spacemodels. *Technical report, Institute of Statistical Mathematics Research Memorandum*(462).

Kitagawa, G. (1996). Monte Carlo filter and smoother for non-Gaussian nonlinear state space models. *Journal of computational and graphical statistics*, *5*(1), 1–25.

Koketsu, K., Miyake, H., & Suzuki, H. (2012). Japan integrated velocity structure model version 1. *Proceedings of the 15th World Conference on Earthquake*

*Engineering*(1773).

Koketsu, K., Miyake, H., Tanaka, Y., et al. (2009). A proposal for a standard procedure of modeling 3-D velocity structures and its application to the Tokyo metropolitan area, Japan. *Tectonophysics*, *472*(1-4), 290–300.

Kostoglodov, V., Husker, A., Shapiro, N. M., Payero, J. S., Campillo, M., Cotte, N., & Clayton, R. (2010). The 2006 slow slip event and nonvolcanic tremor in the Mexican subduction zone. *Geophysical Research Letters*, *37*(24).

Li, S., & Barnhart, W. D. (2020). Impacts of topographic relief and crustal heterogeneity on coseismic deformation and inversions for fault geometry and slip: A case study of the 2015 Gorkha earthquake in the central Himalayan arc. *Geochemistry, Geophysics, Geosystems*, *21*(12), e2020GC009413.

Lindquist, K. G., Engle, K., Stahlke, D., & Price, E. (2004). Global topography and bathymetry grid improves research efforts. *Eos, Transactions American Geophysical Union*, *85*(19), 186–186.

Lindsey, E., & Fialko, Y. (2013). Geodetic slip rates in the southern San Andreas Fault system: Effects of elastic heterogeneity and fault geometry. *Journal of Geophysical Research: Solid Earth*, *118*(2), 689–697.

Maeda, T., & Obara, K. (2009). Spatiotemporal distribution of seismic energy radiation from low-frequency tremor in western Shikoku, Japan. *Journal of Geophysical Research: Solid Earth*, *114*(B10).

Metropolis, N., Rosenbluth, A. W., Rosenbluth, M. N., Teller, A. H., & Teller, E. (1953). Equation of state calculations by fast computing machines. *The journal of chemical physics*, *21*(6), 1087–1092.

Minson, S., Murray, J. R., Langbein, J. O., & Gomberg, J. S. (2014). Real-time inversions for finite fault slip models and rupture geometry based on high-rate GPS data. *Journal of Geophysical Research: Solid Earth*, *119*(4), 3201–3231.

Minson, S., Simons, M., & Beck, J. (2013). Bayesian inversion for finite fault earthquake source models I–Theory and algorithm. *Geophysical Journal International*, *194*(3), 1701–1726.

Miyazaki, S., & Hatanaka, Y. (1998). The outlines of the GEONET (in Japanese). *Meteorol. Res. Note*, *192*, 105–131.

Nakanishi, A., Takahashi, N., Yamamoto, Y., Takahashi, T., Citak, S. O., Nakamura, T., ... Kaneda, Y. (2018). Three-dimensional plate geometry and P-wave velocity models of the subduction zone in SW Japan: Implications for seismogenesis. *Geology and Tectonics of Subduction Zones: A Tribute to Gaku Kimura*, *534*, 69.

Nakata, R., Hino, H., Kuwatani, T., Yoshioka, S., Okada, M., & Hori, T. (2017). Discontinuous boundaries of slow slip events beneath the Bungo Channel, southwest Japan. *Scientific reports*, *7*(1), 6129.

Nakata, R., Kuwatani, T., Okada, M., & Hori, T. (2016). Geodetic inversion for spatial distribution of slip under smoothness, discontinuity, and sparsity constraints. *Earth, Planets and Space*, *68*(1), 1–10.

Obara, K. (2010). Phenomenology of deep slow earthquake family in southwest Japan: Spatiotemporal characteristics and segmentation. *Journal of Geophysical Research: Solid Earth*, *115*(B8).

Obara, K., Hirose, H., Yamamizu, F., & Kasahara, K. (2004). Episodic slow slip events accompanied by non-volcanic tremors in southwest Japan subduction zone. *Geophysical Research Letters*, *31*(23).

Obara, K., & Kato, A. (2016). Connecting slow earthquakes to huge earthquakes. *Science*, *353*(6296), 253–257.

Ozawa, S., Kawabata, R., Kokado, K., & Yarai, H. (2020). Long-term slow slip events along the Nankai trough delayed by the 2016 Kumamoto earthquake, Japan. *Earth, Planets and Space*, *72*, 1–9.

Raftery, A. E., Madigan, D., & Hoeting, J. A. (1997). Bayesian model averaging for linear regression models. *Journal of the American Statistical Association*, *92*(437), 179–191.

Rogers, G., & Dragert, H. (2003). Episodic tremor and slip on the Cascadia subduction zone: The chatter of silent slip. *Science*, *300*(5627), 1942–1943.

Seshimo, Y., & Yoshioka, S. (2021). Spatiotemporal slip distributions of the 2018-2019 Bungo Channel long-term slow slip event. *Japan Geoscience Union Meeting 2021*.

Shimizu, K., Yagi, Y., Okuwaki, R., & Fukahata, Y. (2021). Construction of fault geometry by finite-fault inversion of teleseismic data. *Geophysical Journal International*, *224*(2), 1003–1014.

Swendsen, R. H., & Wang, J.-S. (1986). Replica Monte Carlo simulation of spin-glasses. *Physical review letters*, *57*(21), 2607.

Takagi, R., Uchida, N., & Obara, K. (2019). Along-strike variation and migration of long-term slow slip events in the western Nankai subduction zone, Japan. *Journal of Geophysical Research: Solid Earth*, *124*(4), 3853–3880.

Tibshirani, R., Saunders, M., Rosset, S., Zhu, J., & Knight, K. (2005). Sparsity and smoothness via the fused lasso. *Journal of the Royal Statistical Society: Series B (Statistical Methodology)*, *67*(1), 91–108.

Villafuerte, C., & Cruz-Atienza, V. M. (2017). Insights into the causal relationship between slow slip and tectonic tremor in Guerrero, Mexico. *Journal of Geophysical Research: Solid Earth*, *122*(8), 6642–6656.

Wang, R., Martín, F. L., & Roth, F. (2003). Computation of deformation induced by earthquakes in a multi-layered elastic crust-FORTRAN programs EDGRN/EDCMP. *Computers & Geosciences*, *29*(2), 195–207.

Watanabe, S. (2013). A widely applicable bayesian information criterion. *Journal of Machine Learning Research*, *14*(Mar), 867–897.

Yabuki, T., & Matsu'ura, M. (1992). Geodetic data inversion using a Bayesian information criterion for spatial distribution of fault slip. *Geophysical Journal International*, *109*(2), 363–375. Retrieved from `http://gji.oxfordjournals.org/cgi/doi/10.1111/j.1365-246X.1992.tb00102.x` doi: 10.1111/j.1365-246X.1992.tb00102.x

Yagi, Y., & Fukahata, Y. (2008). Importance of covariance components in inversion analyses of densely sampled observed data: an application to waveform data inversion for seismic source processes. *Geophysical Journal International*, *175*(1), 215–221.

Yagi, Y., & Fukahata, Y. (2011). Introduction of uncertainty of green's function into waveform inversion for seismic source processes. *Geophysical Journal International*, *186*(2), 711–720.

Yamamoto, Y., Obana, K., Takahashi, T., Nakanishi, A., Kodaira, S., & Kaneda, Y. (2013). Imaging of the subducted Kyushu-Palau Ridge in the Hyuga-nada region, western Nankai Trough subduction zone. *Tectonophysics*, *589*, 90–102.

Yoshioka, S., Matsuoka, Y., & Ide, S. (2015). Spatiotemporal slip distributions of three long-term slow slip events beneath the Bungo Channel, southwest Japan, inferred from inversion analyses of GPS data. *Geophysical Journal International*, *201*(3), 1437–1455.